Invariant surface elastic properties in FCC metals via machine learning methods

Xiaolei Chen, Rémi Dingreville, Thiebaud Richeton, Stéphane Berbenni

Invariant surface elastic properties in FCC metals via machine learning methods

Xiaolei Chen[a,c], Rémi Dingreville[b], Thiebaud Richeton[a,c], Stéphane Berbenni[a,c,*]

[a] *Université de Lorraine, CNRS, Arts et Métiers ParisTech, LEM3, F-57000 Metz, France*

[b] *Center for Integrated Nanotechnologies, Nanostructure Physics Department, Sandia National Laboratories, Albuquerque, NM 87185, USA*

[c] *Laboratory of Excellence on Design of Alloy Metals for low-mAss Structures (LabEx DAMAS), Université de Lorraine, Metz, France*

Abstract

We present a combination of machine-learned models that predicts the surface elastic properties of general free surfaces in face-centered cubic (FCC) metals. These models are built by combining a semi-analytical method based on atomistic simulations to calculate surface properties with the artificial neural network or the boosted regression tree method. The latter is also used to link bulk properties and surface orientation to surface properties. The surface elastic properties are represented by their invariants considering plane elasticity within a polar method. The resulting models are shown to accurately predict the surface elastic properties of seven pure FCC metals (Cu, Ni, Ag, Au, Al, Pd, Pt). The BRT model reveals the correlations between bulk and corresponding surface properties in terms of invariants, which can be used to guide the design of complex nano-sized particles, wires and films. Finally, by expressing the surface excess energy density as a function of surface elastic invariants, fast predictions of surface energy as a function of in-plane deformations can be made from these model constructs.

Keywords: Surface elastic properties, surface elastic invariant, molecular statics, machine learning methods

*Corresponding author.

Email address: stephane.berbenni@univ-lorraine.fr (Stéphane Berbenni)

1. Introduction

The theoretical formulation underlying surface elasticity is based on the concept of the Gibbs' dividing surface, in which the thermodynamics of a free surface is formulated in terms of excess quantities relative to the bulk. Within this formalism, the surface excess energy, sometimes also called surface tension[1], is defined as the mechanical work involved with changing the surface area, either when a new area of surface is formed, or when the free surface is elastically stretched. While these two processes are indistinguishable for liquid surfaces, for solid surfaces, Gibbs [1] initially discussed the difference between creating a new surface at constant strain (thermodynamic quantity defined as the surface excess energy density Γ) and straining a solid surface (thermodynamic quantity referred to as the surface stress $\mathbf{\Sigma}^{\mathrm{S}}$). The distinction between Γ and $\mathbf{\Sigma}^{\mathrm{S}}$ is of special importance for nanoparticles, since surface quantities scale as the inverse of the particle size relative to volume quantities. Surface energy, surface stress, and surface elasticity play a central role in the physical properties of nanomaterials including size-dependent mechanical properties [2, 3] and surface melting [4, 5], surface reconstruction [6, 7], surface-driven adsorption [8–10], surface-induced phase transformation [11, 12] or surface self-organization [13, 14].

Because of the importance of surface elastic properties for so many properties in nanomaterials, various approaches have been proposed to measure and predict surface properties. Experimentally, contact-angle measurement [15] is the oldest and most commonly used technique to measure the surface energy, however it cannot measure any other higher-order surface elastic property. Other measurements techniques such as contact atomic force microscopy [16] or resonance frequency measurements [8, 17] provide indirect measurements of those surface elastic properties by measuring the apparent elastic modulus from which residual surface stress and surface elastic moduli can be deduced. Theoretically, the computational methods used to calculate surface properties are based on atomistic simulations, either from first principle (see for instance Ref. [6]) or classical molecular statics (see for instance Ref. [18]) or dynamics (see for instance Ref. [19]). In both cases, these calculations consist first in generating surface orientations with low Miller indices (generally {100}, {110}, and {111} surfaces), and then stretching the simulation cell in the plane of the surface to extract surface properties. As a computation-

[1] To be differentiated from surface tension for liquid interfaces.

ally efficient alternative, we proposed in the past a semi-analytical atomistic method to compute surface elastic properties [20] directly from the relaxed surface configuration without the need to stretch or deform the surface.

The main gap with these experimental and computational methods is that the available data is limited to handful of low Miller indices surface orientations, making it challenging to derive any universal characteristics for the surface elastic properties. Moreover, for anisotropic materials, the Cartesian components of a surface property tensor are frame-dependent parameters, thus making it difficult to compare on an equal footing surface properties among different surface orientations. Besides, the preferred directions linked to the anisotropic properties do not appear explicitly [21]. Hence, similar to the case of the bulk material's properties, there is a need for representing surface tensors as a function of invariants that are independent of reference frame.

In order to extend the analysis of the surface properties to general surface orientations and make them comparable, we use our semi-analytical atomistic method to fastly compute surface elastic properties for a broad range of surface orientations in terms of surface invariants quantities. Results from the semi-analytical atomistic calculation are then used as input into an artificial neural network (ANN) to build a regression model, which can fastly evaluate surface elastic properties as a function of the surface orientation. These results are also used as input in a boosted regression tree (BRT) in order to identify the sensitivity of the surface elastic properties with respect to bulk properties. The manuscript is organized as follows. In Section 2, the surface constitutive behavior is described and the semi-analytical method to compute surface elastic properties is recalled. In Section 3, the polar method introduced by Verchery [22] and the invariants by rotation of surface elastic properties are presented. In Section 4, the ANN and the BRT approaches are presented to construct our surrogate models. In Section 5, we first present the spectrum of surface elastic properties as a function of the surface orientation in 3D plots. Then, we analyze the ability of our surrogate models to predict surface elastic invariants with respect to the surface orientation, as well as the influence of material's bulk properties on these invariants. As an application of the developed models, we also compute the variation of the surface excess energy density with a given in-plane strain mode on different Cu surfaces. Then, Section 6 sketches the conclusions and the perspectives of this work.

2. Semi-analytic method based on Molecular Static (MS) simulations

2.1. Definitions of the Gibbs surface excess energy density, excess stress and excess stiffness

For a semi-infinite crystal, the Lagrangian description of the Gibbs surface excess energy density is expressed as [1, 20]:

$$\Gamma = \frac{1}{A_0}\sum_{n=1}^{\infty}\left(E^{(n)} - E^{(\mathrm{bulk})}\right) \tag{1}$$

where $E^{(n)}$ is the total energy of the atom n and $E^{(\mathrm{bulk})}$ is the total energy of an atom in a perfect lattice far away from the free surface. The area A_0 corresponds to the area measured in the undeformed, relaxed state. Then, the surface elastic constitutive behavior is derived from the Shuttleworth-Herring relation [23–25]. This relation relates the surface excess energy density Γ to the surface stress $\mathbf{\Sigma}^{\mathrm{S}}$ when the surface is elastically strained in the plane of the surface such that [3, 23, 25]:

$$\Sigma^{\mathrm{S}}_{\alpha\beta} = \frac{\partial\Gamma}{\partial\varepsilon^{\mathrm{S}}_{\alpha\beta}} \tag{2}$$

where $\varepsilon^{\mathrm{S}}_{\alpha\beta}$ $(\alpha,\beta = 1,2)$ is the in-plane straining. This two-dimensional relation implicitly accounts for long-range interactions in solids. Assuming that the Gibbs surface excess energy density is a smooth function of the surface strain [3]:

$$\Gamma = \Gamma_0 + \Sigma^0_{\alpha\beta}\varepsilon^{\mathrm{S}}_{\alpha\beta} + \frac{1}{2}\mathbb{C}^{\mathrm{S}}_{\alpha\beta\kappa\lambda}\varepsilon^{\mathrm{S}}_{\alpha\beta}\varepsilon^{\mathrm{S}}_{\kappa\lambda} \tag{3}$$

where Γ_0 is the intrinsic surface excess energy density, $\Sigma^0_{\alpha\beta}$ (with subscripts $\alpha,\beta = 1,2$) is the two-dimensional residual surface stress tensor (also called the intrinsic surface stress tensor) with classic symmetries $\Sigma^0_{\alpha\beta} = \Sigma^0_{\beta\alpha}$, and $\mathbb{C}^{\mathrm{S}}_{\alpha\beta\kappa\lambda}$ (with subscripts $\alpha,\beta,\kappa,\lambda = 1,2$) is the surface elastic stiffness tensor with symmetries $\mathbb{C}^{\mathrm{S}}_{\alpha\beta\kappa\lambda} = \mathbb{C}^{\mathrm{S}}_{\beta\alpha\kappa\lambda} = \mathbb{C}^{\mathrm{S}}_{\alpha\beta\lambda\kappa} = \mathbb{C}^{\mathrm{S}}_{\kappa\lambda\alpha\beta}$. These three quantities are all intrinsic surface elastic properties (*i.e.*, they do not depend on $\varepsilon^{\mathrm{S}}_{\alpha\beta}$), that fully characterize the linear elastic behavior of the surface [20]. Based on the Shuttleworth-Herring relation in Eq. (2), the surface constitutive behavior is therefore defined as:

$$\Sigma^{\mathrm{S}}_{\alpha\beta} = \Sigma^0_{\alpha\beta} + \mathbb{C}^{\mathrm{S}}_{\alpha\beta\kappa\lambda}\varepsilon^{\mathrm{S}}_{\kappa\lambda} \tag{4}$$

Note that Eqs. (2)–(4) are defined with respect to the relaxed state of the free surface, *i.e.* after the free surface has been created and surface atoms have relaxed to their surface atomic positions (which can be different from the perfect lattice configuration).

2.2. Semi-analytical method of surface elastic properties based on MS simulations

Here, we used a semi-analytical atomistic method introduced in [20] to compute the surface elastic properties defined in Eqs. (3) and (4). This method is based on the idea of expanding the energy of a free surface of a discrete atomistic system into power series of the surface strain. This expansion can then be used to derive the intrinsic surface excess energy density Γ_0, the residual surface stress tensor $\Sigma^0_{\alpha\beta}$, and the surface elastic stiffness tensor $\mathbb{C}^{\mathrm{S}}_{\alpha\beta\kappa\lambda}$ (see Eq. (3)) from the relaxed configuration of the free surface. The advantage of this methodology is that the surface properties can be directly derived from the relaxed state of the free surface without the need to perform actual, computationally expensive straining simulations of that surface. The surface elastic properties are formulated analytically and explicitly in terms of the functional form of the used interatomic potential, the embedded atom method (EAM) potential. The relaxed configuration of the free surface is obtained via a single molecular static (MS) simulation.

For a uniform and homogeneous deformation, the Taylor expansion of an interatomic potential function for the atom n in the free surface system (whose normal is directed along the x_3-axis, see Fig. 1) with respect to the relaxed configuration can be written as follows [20]:

$$E^{(n)} = A^{(n)} + A^{(n)}_{ij}\varepsilon_{ij} + \frac{1}{2}A^{(n)}_{ijkl}\varepsilon_{ij}\varepsilon_{kl} \tag{5}$$

where the uniform strain field ε_{ij} is measured from the relaxed state of the free surface system. The scalar quantity $A^{(n)}$ corresponds to an energy per atom and the tensors $A^{(n)}_{ij}$ and $A^{(n)}_{ijkl}$ are derived for each atom n from the functional form of the interatomic potential. In the case of the EAM interatomic potential, which is composed of an embedding-energy term G and a pair-potential term V, the scalar $A^{(n)}$ and the tensors $A^{(n)}_{ij}$ and $A^{(n)}_{ijkl}$ are

defined as [20, 26, 27]:

$$A^{(n)} = G\left(\sum_{m\neq n}\rho\left(\hat{r}^{mn}\right)\right) + \frac{1}{2}\sum_{m\neq n}V\left(\hat{r}^{mn}\right) \tag{6}$$

$$A^{(n)}_{ij} = \left[\sum_{p\neq n}\hat{r}^{pn}_{j}\left(\frac{\partial G}{\partial r^{pn}_{i}} + \frac{1}{2}\frac{\partial V}{\partial r^{pn}_{i}}\right)\Bigg|_{r^{mn}=\hat{r}^{mn}}\right]_{\langle i,j\rangle} \tag{7}$$

$$A^{(n)}_{ijkl} = \left[\sum_{p\neq n}\sum_{q\neq n}\hat{r}^{pn}_{j}\hat{r}^{qn}_{l}\left(\frac{\partial^2 G}{\partial r^{pn}_{i}\partial r^{qn}_{k}} + \frac{1}{2}\frac{\partial^2 V}{\partial r^{pn}_{i}\partial r^{qn}_{k}}\right)\Bigg|_{r^{mn}=\hat{r}^{mn}}\right]_{\langle i,j\rangle,\langle k,l\rangle} \tag{8}$$

where $\hat{r}^{mn}_{i}$ $(i=1,2,3)$ is the position vector between an atom m and atom n in the relaxed configuration of the free surface, while $\hat{r}^{mn}$ is the norm of vector $\hat{r}^{mn}_{i}$ and represents the interatomic distance between atoms m and n, and ρ is the electron density classically defined in the EAM framework. Meanwhile, the $\langle\cdot\rangle$ subscript notation refers to the symmetric part of the base tensor. The analytical expressions of the first and second order spatial derivatives in Eqs. (7) and (8) can be found in [20]. The traction free boundary condition at $x_3 = 0$ writes:

$$\sigma_{13} = \sigma_{23} = \sigma_{33} = 0 \tag{9}$$

Then, based on the linear elastic Hooke's law, any uniform strain field ε_{ij} that is compatible with the condition of Eq. (9) should satisfy the following conditions [20]:

$$\begin{aligned} 2\varepsilon_{13} &= -\mathbb{D}_{1j}\mathbb{C}_{j3\alpha\beta}\varepsilon^{\mathrm{S}}_{\alpha\beta} \\ 2\varepsilon_{23} &= -\mathbb{D}_{2j}\mathbb{C}_{j3\alpha\beta}\varepsilon^{\mathrm{S}}_{\alpha\beta} \\ \varepsilon_{33} &= -\mathbb{D}_{3j}\mathbb{C}_{j3\alpha\beta}\varepsilon^{\mathrm{S}}_{\alpha\beta} \end{aligned} \tag{10}$$

where $\mathbb{C}_{ijkl}$ is the bulk linear elastic stiffness tensor, while $\varepsilon^{\mathrm{S}}_{\alpha\beta}$ $(\alpha,\beta=1,2)$ is the in plane strain tensor, and $\mathbb{D}$ is a linear elastic compliance matrix defined by [20]:

$$\mathbb{D}^{-1} = \begin{pmatrix} \mathbb{C}_{1313} & \mathbb{C}_{1323} & \mathbb{C}_{1333} \\ \mathbb{C}_{2313} & \mathbb{C}_{2323} & \mathbb{C}_{2333} \\ \mathbb{C}_{3313} & \mathbb{C}_{3323} & \mathbb{C}_{3333} \end{pmatrix} \tag{11}$$

Then, using Eq. (10) into Eq. (5) yields [20]:

$$E^{(n)} = A^{(n)} + B^{(n)}_{\alpha\beta}\varepsilon^{\mathrm{S}}_{\alpha\beta} + \frac{1}{2}B^{(n)}_{\alpha\beta\kappa\lambda}\varepsilon^{\mathrm{S}}_{\alpha\beta}\varepsilon^{\mathrm{S}}_{\kappa\lambda} \tag{12}$$

where the tensors $B^{(n)}_{\alpha\beta}$ and $B^{(n)}_{\alpha\beta\kappa\lambda}$ are derived for each atom n as follows [20]:

$$B^{(n)}_{\alpha\beta} = A^{(n)}_{\alpha\beta} - A^{(n)}_{i3}\mathbb{D}_{ij}\mathbb{C}_{j3\alpha\beta} \tag{13}$$

$$\begin{aligned} B^{(n)}_{\alpha\beta\kappa\lambda} =& A^{(n)}_{\alpha\beta\kappa\lambda} + A^{(n)}_{i3j3}\mathbb{D}_{ip}\mathbb{D}_{jq}\mathbb{C}_{p3\alpha\beta}\mathbb{C}_{q3\kappa\lambda} \\ & - A^{(n)}_{i3\kappa\lambda}\mathbb{D}_{iq}\mathbb{C}_{q3\alpha\beta} - A^{(n)}_{\alpha\beta j3}\mathbb{D}_{jp}\mathbb{C}_{p3\kappa\lambda} \end{aligned} \tag{14}$$

Let us note that the "-" signs were corrected with respect to [20] in the last equation. Now, substituting Eq. (12) into Eq. (1) yields [20]:

$$\begin{aligned} \Gamma = \frac{1}{A_0}\sum_{n=1}^{\infty}\Big[& \left(A^{(n)} - A^{(\mathrm{bulk})}\right) + \left(B^{(n)}_{\alpha\beta} - B^{(\mathrm{bulk})}_{\alpha\beta}\right)\varepsilon^{\mathrm{S}}_{\alpha\beta} \\ & + \frac{1}{2}\left(B^{(n)}_{\alpha\beta\kappa\lambda} - B^{(\mathrm{bulk})}_{\alpha\beta\kappa\lambda}\right)\varepsilon^{\mathrm{S}}_{\alpha\beta}\varepsilon^{\mathrm{S}}_{\kappa\lambda}\Big] \end{aligned} \tag{15}$$

where $A^{(\mathrm{bulk})}$, $B^{(\mathrm{bulk})}_{\alpha\beta}$ and $B^{(\mathrm{bulk})}_{\alpha\beta\kappa\lambda}$ are calculated from Eqs. (6), (13) and (14), respectively, for an atom in the bulk far away from the free surface. Thus, comparing Eq. (15) with Eq. (3) leads to the expressions for the surface elastic properties through the semi-analytical method as follows [20]:

$$\Gamma_0 = \frac{1}{A_0}\sum_{n=1}^{\infty}\left(A^{(n)} - A^{(\mathrm{bulk})}\right) \tag{16}$$

$$\Sigma^0_{\alpha\beta} = \frac{1}{A_0}\sum_{n=1}^{\infty}\left(B^{(n)}_{\alpha\beta} - B^{(\mathrm{bulk})}_{\alpha\beta}\right) \tag{17}$$

$$\mathbb{C}^{\mathrm{S}}_{\alpha\beta\kappa\lambda} = \frac{1}{A_0}\sum_{n=1}^{\infty}\left(B^{(n)}_{\alpha\beta\kappa\lambda} - B^{(\mathrm{bulk})}_{\alpha\beta\kappa\lambda}\right) \tag{18}$$

where A_0 is the surface area of the free surface in its relaxed state.

The open-source molecular dynamics simulation code LAMMPS [28] (Large-scale Atomic/Molecular Massively Parallel Simulator) was used to perform all the MS simulations. We used seven EAM potentials to describe the interatomic interactions in silver (Ag), gold (Au), copper (Cu), nickel (Ni), palladium (Pd), platinum (Pt) [29], and aluminum (Al)[30]. These potentials are fit to give the bulk elastic constants, cohesive energy, low-index surface energies, and stacking fault energy. These potentials have been successfully used in other studies to simulate the mechanical behavior of nanostructures [31–35].

We simulated the initial unrelaxed free surface configurations by rotating a perfect crystal lattice to end up with the desired surface orientation within a rectangular simulation cell. We used periodic boundary conditions in the in-plane directions (*i.e.* x_1-x_2 plane in Fig. 1 (a)) in order to mimic an infinite film. In the normal direction to the free surface (*i.e.* the x_3-direction), the thickness of the film was chosen sufficiently large to ensure that our results are independent of the film thickness (see Fig. 1 (a)). The dimensions of the computational domain was selected to be $30 \times 30 \times 15$ nm^3 as shown in Fig. 1 (a). Upon the creation of the free surfaces, the atomistic system was relaxed using a conjugate gradient energy minimization. We used a cropped-up sub-cell of dimensions $15 \times 15 \times 15$ nm^3 in order to mitigate any boundary effects when calculating the surface properties with the semi-analytical method as shown in Fig. 1 (b). The selected dimension of the initial system and the sub-cell were set to be large enough to ensure the convergence of the numerical results. The bulk material was considered to be the middle part of the sub-cell with a thickness $\mathrm{H_{Bulk}} = 5$nm as shown in Fig. 1 (c), which was used to determine the variables $A^{(\mathrm{Bulk})}$, $B^{(\mathrm{Bulk})}_{\alpha\beta}$ and $B^{(\mathrm{Bulk})}_{\alpha\beta\kappa\lambda}$ in Eqs. (16) - (18), respectively. Meanwhile, the effective surface layer, used to determine the variables $A^{(n)}$, $B^{(n)}_{\alpha\beta}$ and $B^{(n)}_{\alpha\beta\kappa\lambda}$ in Eqs. (16) - (18), was determined via an energy consideration. First, the sub-cell was divided into layers with a thickness of 0.1 nm in the x_3-direction. Then, the surface layer was considered to be the sum of all the top layers until the relative difference of the average atom energy between two adjacent layers was smaller than 10^{-3} times the one of the bulk material ($\Delta E_i < 10^{-3} E^{(\mathrm{Bulk})}$ as shown in Fig. 1 (c)).

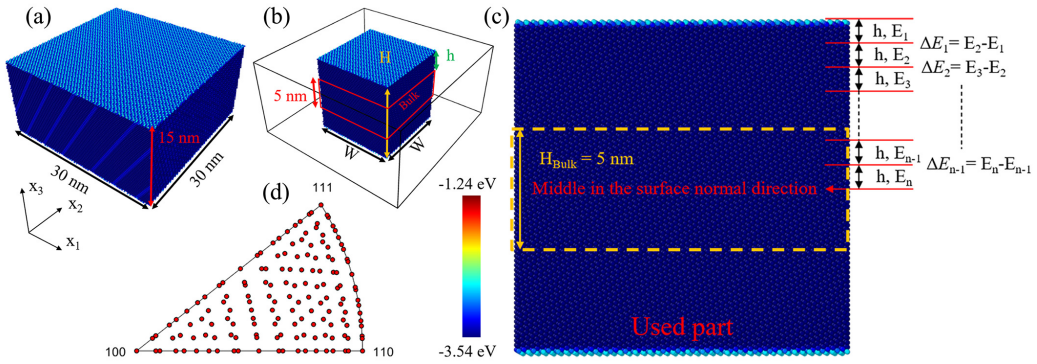

Figure 1: Schematic of (a) the initial MS simulation box, (b) the sub-cell used in the semi-analytical method, (c) the strategy of surface layer determination and (d) 151 uniformly distributed surface orientations presented in the inverse pole figure (IPF).

3. Polar method and surface invariant properties by rotation

3.1. Invariants by rotation of surface tensors $\Sigma^0_{\alpha\beta}$ and $\mathbb{C}^S_{\alpha\beta\kappa\lambda}$

For tensorial properties such as the residual surface stress tensor $\Sigma^0_{\alpha\beta}$ and the surface stiffness tensor $\mathbb{C}^S_{\alpha\beta\kappa\lambda}$, the values of the different Cartesian components are dependent on the chosen Cartesian frame, which impedes direct comparisons between different surface orientations. Therefore, the surface elastic properties, *i.e.* $\Sigma^0_{\alpha\beta}$ and $\mathbb{C}^S_{\alpha\beta\kappa\lambda}$ present in Eq. (4) are represented in this work by invariants by rotation, following the so-called polar method in plane elasticity. This method is a mathematical method based upon a complex variable change introduced by Verchery [22]. This method was previously used in the mechanics community for investigating the elastic behavior of anisotropic composite laminates and planar orthotropic materials [36–39].

First, the Cartesian components of the second order tensor $\Sigma^0_{\alpha\beta}$ can be represented by the polar components T, R, Φ defined as [37]:

$$\begin{aligned} \Sigma^0_{11} &= T + R\cos 2\Phi \\ \Sigma^0_{22} &= T - R\cos 2\Phi \\ \Sigma^0_{12} &= R\sin 2\Phi \end{aligned} \tag{19}$$

T and R are the two invariants of the tensor $\Sigma^0_{\alpha\beta}$ and represent its spherical and deviatoric parts, respectively. T and R are thus two intrinsic invariant properties by rotation of the surface. It is noteworthy to mention that T

is half of the trace of $\Sigma^0_{\alpha\beta}$ and R can be interpreted as the radius of the Mohr circle (see Eqs. (A.1) in Appendix A). Meanwhile, Φ is a polar angle reflecting the rotation around the x_3-axis in the Cartesian frame (x_1, x_2, x_3) from the principal frame of $\Sigma^0_{\alpha\beta}$. The explicit formula of Φ is expressed by Eq. (A.2) in Appendix A.

Second, the Cartesian components of the fourth-order tensor $\mathbb{C}^{\mathrm{S}}_{\alpha\beta\kappa\lambda}$ can be represented by the polar components T_0, T_1, R_0, R_1, Φ_0, Φ_1 defined as [37]:

$$\begin{aligned}
\mathbb{C}^{\mathrm{S}}_{1111} &= 2T_1 \quad +4R_1\cos 2\Phi_1 + T_0 \quad +R_0\cos 4\Phi_0 \\
\mathbb{C}^{\mathrm{S}}_{2222} &= 2T_1 \quad -4R_1\cos 2\Phi_1 + T_0 \quad +R_0\cos 4\Phi_0 \\
\mathbb{C}^{\mathrm{S}}_{1122} &= 2T_1 \quad\quad\quad\quad\quad\quad - T_0 \quad -R_0\cos 4\Phi_0 \\
\mathbb{C}^{\mathrm{S}}_{1212} &= \quad\quad\quad\quad\quad\quad\quad + T_0 \quad -R_0\cos 4\Phi_0 \\
\mathbb{C}^{\mathrm{S}}_{1112} &= \quad\quad +2R_1\sin 2\Phi_1 \quad\quad\quad +R_0\sin 4\Phi_0 \\
\mathbb{C}^{\mathrm{S}}_{2212} &= \quad\quad +2R_1\sin 2\Phi_1 \quad\quad\quad -R_0\sin 4\Phi_0
\end{aligned} \tag{20}$$

where T_1, R_1, T_0 and R_0 are four invariants of the tensor $\mathbb{C}^{\mathrm{S}}_{\alpha\beta\kappa\lambda}$. T_1 and T_0 are the isotropic parts of $\mathbb{C}^{\mathrm{S}}_{\alpha\beta\kappa\lambda}$ while R_1 and R_0 are the corresponding anisotropic parts [37]. Similar to Φ for $\Sigma^0_{\alpha\beta}$, the two polar angles Φ_1 and Φ_0 are rotation angles from two reference frames that can be associated with $\mathbb{C}^{\mathrm{S}}_{\alpha\beta\kappa\lambda}$ (see the description of generalized Mohr's circles for $\mathbb{C}^{\mathrm{S}}_{\alpha\beta\kappa\lambda}$ in [37]). Hence, the difference between Φ_0 and Φ_1 is a constant value since it represents an invariant describing the angle between two reference frames that are specific to $\mathbb{C}^{\mathrm{S}}_{\alpha\beta\kappa\lambda}$. Therefore, there are five invariants (T_1, R_1, T_0, R_0, $\Phi_0 - \Phi_1$) for the tensor $\mathbb{C}^{\mathrm{S}}_{\alpha\beta\kappa\lambda}$ [37]. The explicit formulas of these polar components $(T_1, R_1, T_0, R_0, \Phi_1, \Phi_0)$ are expressed by Eqs. (A.3)-(A.4) in Appendix A.

Now, considering a frame rotation around the x_3-axis with an amplitude Φ_{r}, the three polar angles are expressed in the new frame by: $\Phi' = \Phi - \Phi_{\mathrm{r}}$, $\Phi'_0 = \Phi_0 - \Phi_{\mathrm{r}}$ and $\Phi'_1 = \Phi_1 - \Phi_{\mathrm{r}}$, where Φ, Φ_0, Φ_1 are the values in the original frame [37]. The differences between the polar angle Φ for $\Sigma^0_{\alpha\beta}$ and the polar angles Φ_0 and Φ_1 for $\mathbb{C}^{\mathrm{S}}_{\alpha\beta\kappa\lambda}$ in the new frame can be calculated as follows:

$$\begin{aligned}
\Phi'_1 - \Phi' &= (\Phi_1 - \Phi_{\mathrm{r}}) - (\Phi - \Phi_{\mathrm{r}}) \quad = \Phi_1 - \Phi \\
\Phi'_0 - \Phi' &= (\Phi_0 - \Phi_{\mathrm{r}}) - (\Phi - \Phi_{\mathrm{r}}) \quad = \Phi_0 - \Phi
\end{aligned} \tag{21}$$

The differences between these polar angles in the new frame are the same as in the original frame, meaning that these two angular differences are also invariant properties by rotation for the surface. However, combined with

$\Phi_0 - \Phi_1$, there are only two independent quantities among these three surface invariant properties. In the present paper, we consider $\Phi_1 - \Phi$ and $\Phi_0 - \Phi_1$ to be the two independent surface invariant properties (then $\Phi_0 - \Phi = \Phi_0 - \Phi_1 + \Phi_1 - \Phi$). We choose their smallest absolute values as their amplitude. Meanwhile, we use the convention that these invariants are positive in the clockwise direction and negative in the counterclockwise direction as shown in Fig. 2. From Eq. (19), it is seen that the components of $\Sigma^0_{\alpha\beta}$ remain the same by changing Φ into $\Phi + 180°$ (see also Fig. 2 (a) for a geometric interpretation). Similarly, from Eq. (20) the components of $\mathbb{C}^{\mathrm{S}}_{\alpha\beta\kappa\lambda}$ remain the same by changing Φ_1 into $\Phi_1 + 180°$ and/or Φ_0 into $\Phi_0 + 90°$ (see Fig. 2 (a) and (b) for a geometric interpretation). Then, it can be found that $\Phi_1 - \Phi$ is in the range $]-90°, 90°]$ and the configuration with $\Phi_1 - \Phi$ close to $-90°$ is similar to the configuration with $\Phi_1 - \Phi$ close to $90°$. Similarly, $\Phi_0 - \Phi_1$ is in the range $]-45°, 45°]$ and the case of $\Phi_0 - \Phi_1$ close to $-45°$ is similar to the one with $\Phi_0 - \Phi_1$ close to $45°$.

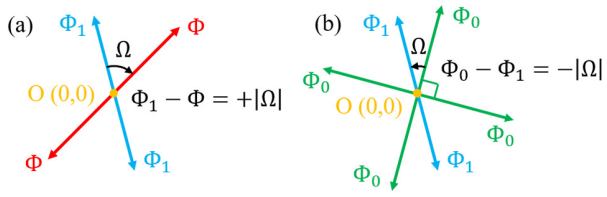

Figure 2: Schematic figures of the two considered surface elastic angular invariants: (a) $\Phi_1 - \Phi$ and (b) $\Phi_0 - \Phi_1$.

Moreover, for an anisotropic surface characterized by non-zero R_0 and R_1, the case of orthotropic symmetry can be expressed by the following condition [37]:

$$\Phi_0 - \Phi_1 = K\frac{\pi}{4} \tag{22}$$

where K can be set to 0 or 1. These two values correspond to two different types of surface orthotropy [36].

As a summary, including all above mentioned surface elastic invariants (T, R, T_1, R_1, T_0, R_0, $\Phi_0 - \Phi_1$, $\Phi_1 - \Phi$) and Γ_0 (scalar quantity), there are in total 9 intrinsic invariant surface elastic properties to describe the surface elastic behavior. In the present paper, all these invariant surface elastic properties are classified into two categories. The first category is called

"surface elastic non-angular parameters" which includes Γ_0, T, R, T_1, R_1, T_0 and R_0. The second category is called "surface elastic angular parameters", including $\Phi_0 - \Phi_1$ and $\Phi_1 - \Phi$, for which the values are periodic. This classification is important for the application of machine-learning methods, as the surface elastic non-angular parameters can be directly applied with the regression method, while the surface elastic angular parameters cannot due to their periodicity. For the periodic data, such as an angle or a date/time, a discrete classification-regression machine-learning method is needed for the prediction (see more details in Section 4).

3.2. Evaluation of the surface excess energy density Γ based on invariant surface elastic properties

Let us now consider a strain loading of the surface defined by an in-plane strain $\varepsilon^{\mathrm{S}}_{\alpha\beta}$ which can be expressed by its polar components t, r and ψ in the Cartesian frame (x_1, x_2, x_3) as follows [37]:

$$\begin{aligned} \varepsilon^{\mathrm{S}}_{11} &= t + r\cos 2\psi \\ \varepsilon^{\mathrm{S}}_{22} &= t - r\cos 2\psi \\ \varepsilon^{\mathrm{S}}_{12} &= r\sin 2\psi \end{aligned} \tag{23}$$

Then, considering the expressions of $\Sigma^0_{\alpha\beta}$ (Eq. (19)) and $\mathbb{C}^{\mathrm{S}}_{\alpha\beta\kappa\lambda}$ (Eq. (20)) at the same point, the surface excess energy density Γ given by Eq. (3) yields:

$$\begin{aligned} \Gamma =& \Gamma_0 + 2Tt + 2Rr\cos 2\left(\Phi - \psi\right) \\ &+ 4T_1 t^2 + 8R_1\cos 2\left(\Phi_1 - \psi\right) tr + 2\left[R_0\cos 4\left(\Phi_0 - \psi\right) + T_0\right] r^2 \end{aligned} \tag{24}$$

The term $2Tt + 2Rr\cos 2\left(\Phi - \psi\right)$ is related to $\Sigma^0_{\alpha\beta}$ whereas the term $4T_1 t^2 + 8R_1\cos 2\left(\Phi_1 - \psi\right) tr + 2\left[R_0\cos 4\left(\Phi_0 - \psi\right) + T_0\right] r^2$ is related to $\mathbb{C}^{\mathrm{S}}_{\alpha\beta\kappa\lambda}$. The rotation angle ψ between the principal frame of $\varepsilon^{\mathrm{S}}_{\alpha\beta}$ and the frame (x_1, x_2, x_3) can be specified with respect to the principal frame of $\Sigma^0_{\alpha\beta}$ with an amplitude Δ as follows:

$$\psi = \Phi + \Delta \tag{25}$$

In the present manuscript, we consider 6 in-plane strain modes with an amplitude ε which are given in the principal frame of $\varepsilon^{\mathrm{S}}_{\alpha\beta}$ (*i.e.*, considering that the Cartesian frame (x_1, x_2, x_3) is such that $\psi = 0$) by:

I. Uniaxial compressive strain:

$$t = -\frac{\varepsilon}{2}, r = -t \tag{26}$$

II. Uniaxial tensile strain:

$$t = \frac{\varepsilon}{2}, r = t \tag{27}$$

III. Equibiaxial compressive strains:

$$t = -\varepsilon, r = 0 \tag{28}$$

IV. Equibiaxial tensile strains:

$$t = \varepsilon, r = 0 \tag{29}$$

V/VI. Positive/Negative shear deformation:

$$t = 0, r = \varepsilon \tag{30}$$

For instance, we will have an uniaxial tensile strain ($r = t$) along the first principal direction of $\Sigma^0_{\alpha\beta}$ for $\psi = \Phi$ while for $\psi = \Phi + 90°$, it will be along the second principal direction of $\Sigma^0_{\alpha\beta}$. However, an uniaxial compressive strain ($r = -t$), will be along the second principal direction of $\Sigma^0_{\alpha\beta}$ for $\psi = \Phi$ and for $\psi = \Phi + 90°$, it will be along the first principal direction of $\Sigma^0_{\alpha\beta}$. In the same way, a shear ($t = 0$) along the first principal direction of $\Sigma^0_{\alpha\beta}$ will be obtained for $\psi = \Phi - 45°$, which is here called "positive shear". In order to reverse the sense of shear which is defined as "negative shear" in the present paper, one must set $\psi = \Phi + 45°$ since r, as a complex number magnitude [37], is always positive. Once the imposed strain is defined, the surface excess energy density Γ (Eq. (24)) only depends on 9 invariant surface elastic properties (Γ_0, T, R, T_1, R_1, T_0, R_0, $\Phi_1 - \Phi$, $\Phi_0 - \Phi_1$).

4. Machine learning methods

In the present contribution, we used two machine-learning methods: ANN (Artificial Neural Network) and BRT (Boosted Regression Tree), to build surrogate models that predict surface properties according to the surface orientation. ANN is an algorithmic mathematical method that imitates the behavior characteristics of biological neural network and carries out information processing. In the ANN method, unit nodes are used to simulate neurons, and the purpose of processing information is achieved by adjusting the weights of interconnections between a large number of nodes (neurons)

in the neural network. The ANN method has been used to solve a variety of problems, such as the image recognition [40] and the text recognition [41]. Recently, the ANN method has also been used for investigating the mechanical properties of materials [42]. Meanwhile, the BRT method is an ensemble-learning method that combines regression trees [43] with boosting [44]. Regression trees are models that relate a metered response to their descriptors using recursive, binary splits. Boosting is an adaptive method that combines many simple models (regression trees in this case) using techniques such as stacking and model averaging for instance. In other words, coupling decision trees with boosting corresponds to add new trees iteratively, in order to improve the predictions of the model for the observations that are poorly predicted by the existing, previous collection of trees. Furthermore, the BRT method can also classify the importance of input factors for the target. In the present manuscript, the ANN method is used to link the surface orientation to surface elastic properties, while the BRT method is used for a sensitivity analysis to identify the sensitivity of surface properties with respect to bulk crystal properties.

4.1. Artificial Neural Network (ANN)

We constructed regression models in order to predict invariant surface elastic properties with respect to the surface orientation using the ANN algorithm [45]. The ANN regression method was directly applied to the surface elastic non-angular parameters, while the surface elastic angular parameters cannot be directly predicted by the regression method. Based on the previous analyses in Fig. 2, the surface elastic angular parameters are circular data, which are in a non-Euclidean space and have a periodic influence for the regression method. For example, the configuration with $\Phi_1 - \Phi$ close to $-90°$ is similar to the case of $\Phi_1 - \Phi$ close to $90°$. However, these cases can be vastly different for the regression method. Therefore, it brings some indetermination in the regression method. In order to predict continuous circular data for surface elastic angular parameters, a discrete-classification conversion method [46, 47] was used. The principle of this method is to discretize the periodic range $(]-90°, 90°]$ for $\Phi_1 - \Phi$ and $]-45°, 45°]$ for $\Phi_0 - \Phi_1)$ into N unique parts and convert the continuous regression task into a N-label classification task. In order to reduce the precision loss introduced by the discretization, the classification task was divided into M groups considering a different starting value for each discretization. After that, the probability densities for $N \times M$ unique orientations were calculated using the von-Mises

distribution as a kernel function and combined with corresponding softmax probabilities [48] (outputs of the softmax function which is used in the final layer of a neural network-based classifier). The von-Mises distribution refers to a continuous model of probability distribution on a circle, based on a concentration parameter ν, which represents the concentration of azimuth. It is also called an approximation of the circular normal distribution or the wrapped normal distribution, as it is a cyclic simulation of the normal distribution. Then, the final prediction was chosen to be the angle with the highest probability density (see more details in [47]). In order to determine the softmax probabilities for the classification task, the ANN classification method was used. There is a potential issue with the discrete-classification conversion method as the discretization step can cause the loss of information, which is the angular precision. However, Hara et al. [47] have showed that a discretization of $N = 8$ and $M = 9$ can already successfully recover the continuous angular data in the range $]0, 360°]$ (the angular precision being $5°$) for the determination of the direction with 2358 training samples, and without the need for further discretization.

We chose the surface orientation as the input factors for the developed ANN models. The surface orientation was represented by two spherical coordinates ϕ and θ as shown in Fig. 3 (b). Meanwhile, we considered 7 FCC representative materials (Ag, Al, Cu, Au, Ni, Pd, Pt) and we created 2128 different surface configurations as the database, with 304 surface orientations for each material as shown in Fig. 3 (a). Then, we trained an ANN model for each invariant surface elastic property of each studied material with the corresponding database. Therefore, for the surface elastic non-angular parameters, there were a total of 7×7 ANN regression models. However, for each surface elastic angular parameter, there were $7 \times M$ (M groups with N-label classification task in each group for one material) $= 7M$ ANN classification models. Furthermore, 80% of the database was randomly chosen to be the training set and the remaining 20% of the database was set to be the testing set.

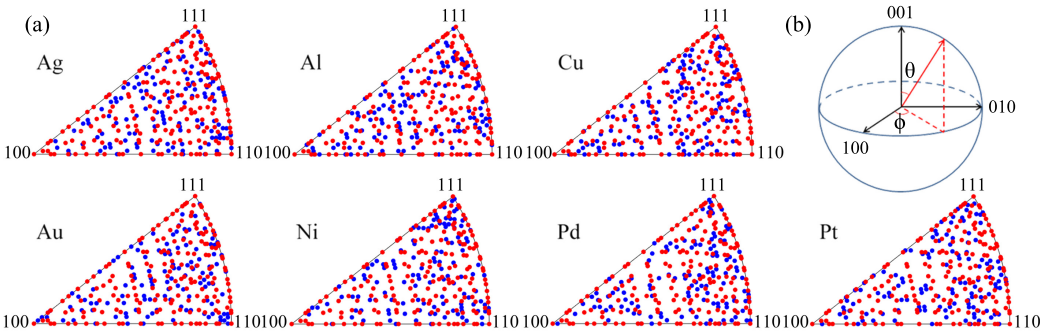

Figure 3: (a) Surface orientations used in machine-learning methods presented in the IPF, with the unique ones for each material marked in blue (125) and the common ones among all the materials marked in red (179). (b) The surface orientation is represented by its spherical coordinates ϕ and θ.

We used the Matlab Neural Network Fitting Application [49] to construct our ANN models. An ANN model is defined by the number of hidden layers and the number of neurons in each hidden layer as shown in Fig. 4. There were 2 hidden layers with 5 neurons in each layer for the ANN regression models and 3 hidden layers with 15 neurons in each layer for the ANN classification models. Moreover, the discretization parameters and the concentration parameter used for predicting the surface elastic angular parameters were optimized to be $N = 12$, $M = 15$, $\nu = 0.0001$ for $\Phi_1 - \Phi$ and $N = 9$, $M = 10$, $\nu = 0.0001$ for $\Phi_0 - \Phi_1$. The angular precision was 1° for these two angular invariants.

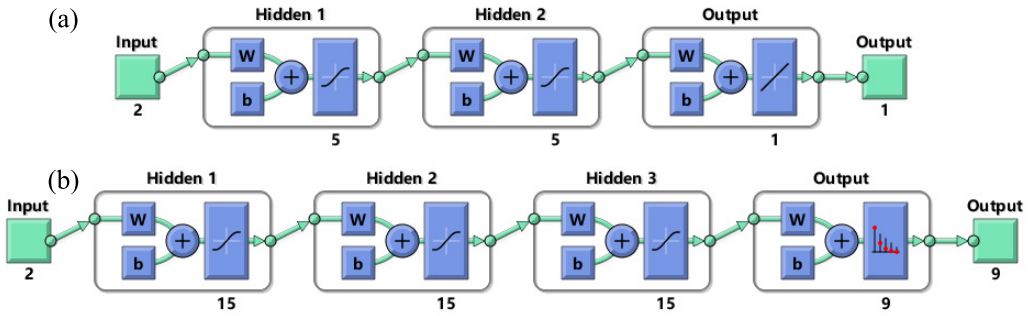

Figure 4: Schematic diagram of (a) an ANN regression model with 2 hidden layers and 5 neurons in each layer used for surface elastic non-angular parameters (1 output corresponds to each surface elastic non-angular parameter of one studied material) and (b) an ANN classification model with 3 hidden layers and 15 neurons in each layer used for predicting $\Phi_0 - \Phi_1$ (9 outputs correspond to $N = 9$ labels classification task) [49]. The 2 input factors correspond to the surface orientation defined by angles ϕ and θ.

4.2. Boosted Regression Tree (BRT)

As a comparison and in order to analyze as well the influence of the bulk crystal properties on the surface elastic non-angular parameters, we also constructed regression models using the BRT algorithm [50, 51] with the same database as shown in Fig. 3 (a). In contrast with the previous ANN models, besides the surface orientation defined by angles ϕ and θ (see Fig. 3 (b)), we also chose 7 material's bulk parameters as input factors in order to analyze their importance for the prediction of the surface elastic non-angular parameters. The 7 material's bulk parameters are: the lattice parameter (a), the stacking fault energy (SFE), the cohesive energy (CHE), the bulk modulus ($K = \frac{1}{3}(\mathbb{C}_{1111} + 2\mathbb{C}_{1122})$), the $\{001\}\langle 110\rangle$ shear resistance ($G' = \frac{1}{2}(\mathbb{C}_{1111} - \mathbb{C}_{1122})$), the $\{001\}\langle 100\rangle$ shear resistance ($G'' = \mathbb{C}_{2323}$) [52] and the elastic anisotropy ratio (Zener coefficient) ($A = \frac{G''}{G'}$), where $\mathbb{C}_{ijkl}$ is the elastic stiffness tensor of the bulk material. The value of these 7 material's parameters for the 7 studied materials are presented in Fig. 5. In conclusion, there were 9 input factors for the developed BRT models. Meanwhile, these BRT models were individually trained for each of the 7 surface elastic non-angular parameters considering all the studied materials together. So, there were in total 7 machine-learned BRT models.

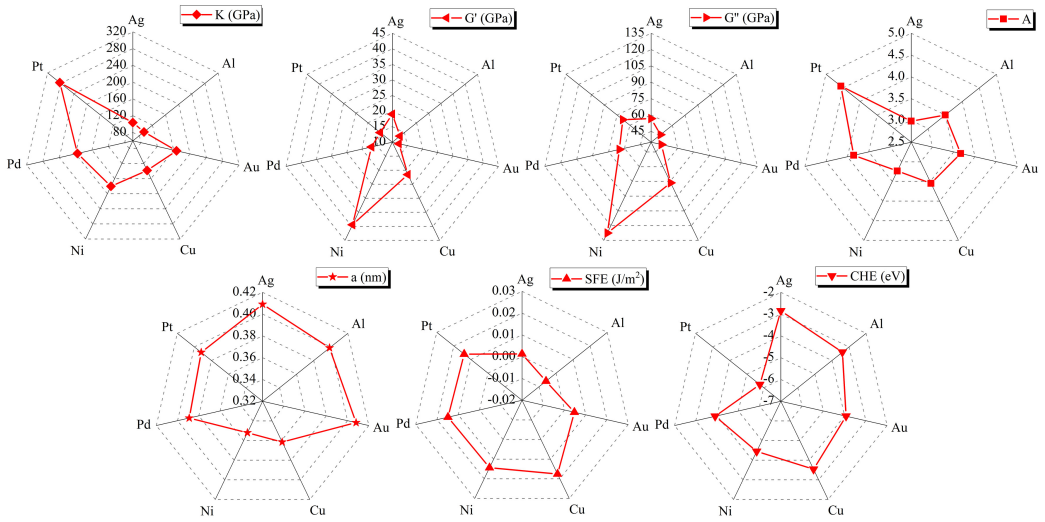

Figure 5: Material's bulk parameters: K (the bulk modulus, in GPa), G' (the $\{001\}\langle 110\rangle$ shear resistance, in GPa), G'' (the $\{001\}\langle 100\rangle$ shear resistance, in GPa), A (the elastic anisotropy ratio), a (the lattice parameter, in nm), SFE (the stacking fault energy, in $\mathrm{J/m^2}$) and CHE (the cohesive energy, in eV) used in BRT models for all the studied materials.

We used the implementation of the boosting algorithm AdaBoost [53] in *Scikit-learn* [54]. The hyperparameters used to define our BRT were: the learning rate parameter, the number of trees, the regularization term, and the maximum number of terminal nodes in a given tree called "leafs". First, we fixed the maximum number of leafs to the default value of 10. We optimized the rest of the hyperparameters to yield the best five-fold cross-validation error on the training data sets using a grid-search optimization strategy. The selected values are listed in Table 1. Furthermore, in *Scikit-learn* [54], the importance of input factors for the target is the impurity-based factor importance, also known as the "Gini" importance, which is computed as the total reduction of the error caused by this factor. The higher the score, the more important the factor should be. The sum of all the scores is equal to 1.

Surface elastic non-angular parameters / Hyper-parameters	Γ_0	T	R	T_1	R_1	T_0	R_0
Loss function	exponential	square	exponential	exponential	linear	square	square
Estimator number	350	200	250	400	300	350	350
Learning rate	1	0.1	0.05	0.5	1	1	0.75
Score method	R2	MSE	R2	R2	R2	R2	R2

Table 1: Best five-fold cross-validated BRT hyperparameters used for each surface elastic non-angular parameter.

5. Results and discussions

5.1. Spectrum of invariant surface elastic properties for FCC free surfaces

In this section, the relaxed surface elastic properties for the 7 studied FCC materials with 151 distinct surface orientations (see Fig. 1 (d)) are computed by the semi-analytical method and then represented by 3D surface plots with variations of surface orientation. Moreover, the results for the unrelaxed Cu surfaces are also presented in order to study the effects of the atomic relaxation.

5.1.1. Intrinsic surface excess energy density Γ_0

For comparison, the analytical method of Herring [55] to determine Γ_0 for an unrelaxed surface of a crystalline material is considered. The latter is based on a linear combination of Γ_0 for three non-coplanar surface orientations as follows:

$$\Gamma_0 = f^1\Gamma_0^1 + f^2\Gamma_0^2 + f^3\Gamma_0^3 \tag{31}$$

where Γ_0^i $(i = 1, 2, 3)$ are the intrinsic surface excess energy density for three reference surfaces and f^i $(i = 1, 2, 3)$ are the corresponding linear coefficients. These coefficients can be determined as follows:

$$\boldsymbol{n} = f^1\boldsymbol{n}^1 + f^2\boldsymbol{n}^2 + f^3\boldsymbol{n}^3 \tag{32}$$

where $\boldsymbol{n}^i$ $(i = 1, 2, 3)$ are the unit normal vector of the three reference surfaces and $\boldsymbol{n}$ is the one of the studied surface. The distribution of Γ_0 in the crystallographic orientation space were calculated for Ni from the Herring's

method (see Fig. 6 (a)) by considering the three reference surface orientations as {100}, {110}, {111} and computing the corresponding Γ_0 values by the semi-analytical method (Eq. (16)). Meanwhile, the distribution of Γ_0 for Ni relaxed surfaces entirely calculated by the semi-analytical method is presented in Fig. 6 (b) and the differences between these two methods are presented in Fig. 6 (c). It is found that the results of the Herring's method agree well with the ones of the complete semi-analytical method, even considering the atomic relaxation.

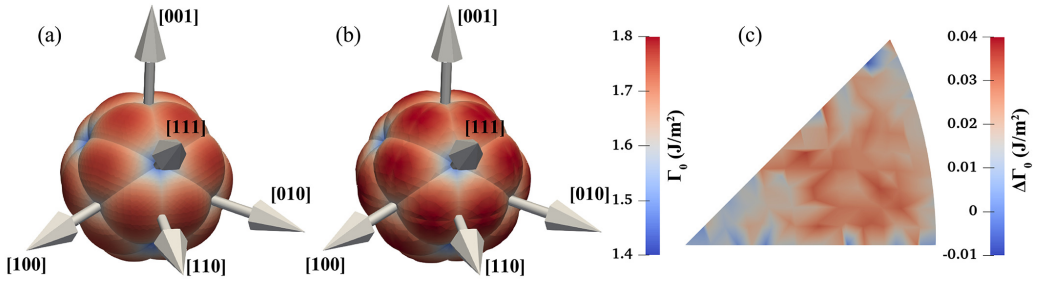

Figure 6: 3D surface plots of Γ_0 for Ni free surfaces calculated by (a) Herring's method without atomic relaxation [55] and (b) semi-analytical method considering atomic relaxation, (c) IPF representation of the difference of Γ_0 between (b) and (a) presented in the IPF.

Figure 7 shows the distribution of Γ_0 for the 7 studied materials and considers also the effects of the atomic relaxation for Cu surfaces as an example. It can be found that the atomic relaxation does not affect very much the values of Γ_0. Comparing the results for different materials, the form of Γ_0 with the surface orientation variation in the 3D view is similar, but it is not homothetic as for example reported in [56]. Indeed, the ratio between the values of Γ_0 for two specific surface orientations is not the same for all the considered materials (see for example the ratio between {110} and {111} surfaces for the 7 studied materials, presented in Table B.1 in Appendix B). However, these ratios are very close, with a relative difference smaller than 7% among all the considered materials. For each material, the value of Γ_0 for 3 specific surface orientations {100}, {110} and {111} are always with the same ranking: $\{110\} > \{100\} > \{111\}$ (cf. Table B.1 in Appendix B). Meanwhile, for each material, {111} surfaces exhibit the smallest values of Γ_0. The behavior of Γ_0 is anisotropic, but its shape as reported in Fig. 7 indicates smooth variations with the surface orientation. According to Table

B.1 in Appendix B, the numerical values of Γ_0 are consistent with the ones reported by Dingreville and Qu [20] regarding these specific orientations.

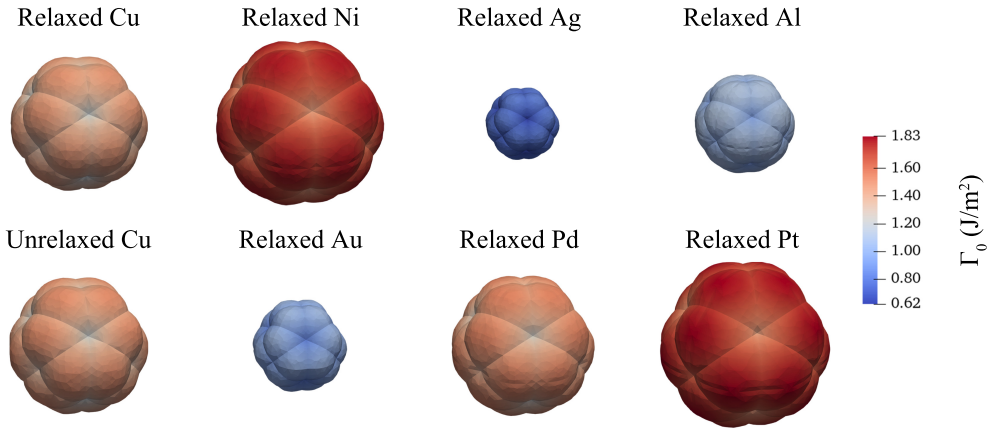

Figure 7: 3D surface plots of Γ_0 for the 7 studied materials. For a sake of clarity, the coordinates axis are omitted but are at the same positions as shown in Figs. 6 (a-b). The size of these 3D plots is proportional to the corresponding amplitude of Γ_0.

5.1.2. Residual surface stresses described by T and R

The distributions of residual surface stress invariants T and R are reported in Fig. 8. Unlike Γ_0, the atomic relaxation has a strong influence on these two invariants. During the relaxation of the surface atomic configuration, there is a reduction of the surface residual stresses. Therefore, the atomic relaxation has a significant influence on the two invariants T and R. The atomic relaxation slightly changes the angular dependence of T and makes its variation sharper for Cu. However, the influence of atomic relaxation is more important on R: it increases the magnitude of R for Cu in the surface orientations lying on the arc from [100] to [111], while it reduces it on the arc from [100] to [110]. These two invariants also show strong anisotropic behaviors. In contrast with Γ_0, their forms exhibit sharp variations. From a comparison among different studied FCC materials and after relaxation, their orientation dependence can be roughly classified into two groups, with the first group including Cu, Ag, Al and Ni and the second group including Au, Pd and Pt. In each group, the orientation dependence is similar but not the amplitudes. Moreover, it is found that T is always positive throughout the orientation space for all the 7 considered materials, which means the free surface is always in a tensile biaxial residual stress state, and so the surfaces

tend to contract within the surface plane [20]. The values of T and R for 3 specific surface orientations {100}, {110} and {111} of all the 7 studied materials are presented in Table B.2 and B.3, respectively, in Appendix B.

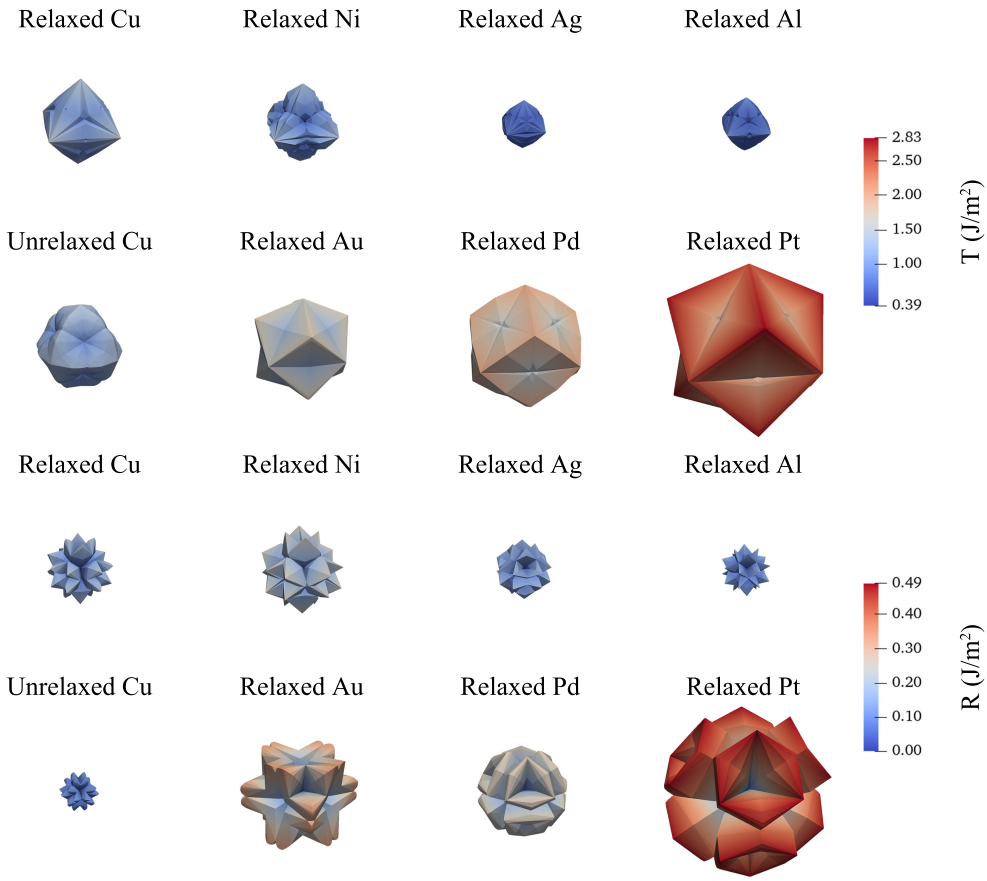

Figure 8: 3D surface plots of residual surface stress invariants for the 7 studied materials. For a sake of clarity, the coordinates axis are omitted but are at the same positions as shown in Figs. 6 (a-b). The size of these 3D plots is proportional to the corresponding amplitude of T and R.

5.1.3. Surface elastic stiffnesses described by T_0, R_0, T_1 and R_1

The results of surface elastic stiffness non-angular invariants are presented in Fig. 9-10. The atomic relaxation influences these 4 invariants. It does not change their orientation dependence for Cu, but reduces their amplitude except for the surface orientations on the arc from [100] to [111] for T_1. Similar to T and R, the form of these 4 invariants after relaxation can be

classified into the same two groups, with Ag, Al, Cu and Ni in the first group and Au, Pd and Pt in the second group. In each group the form of these 4 invariants is similar among different materials but the magnitude is different. These 4 invariants also show strong anisotropic behavior and their forms exhibit sharp variations. Furthermore, T_0 and T_1 are not always positive [19, 20]. Unlike the elastic stiffness tensor of the bulk material, the surface elastic stiffness tensor $\mathbb{C}^{\mathrm{S}}_{\alpha\beta\kappa\lambda}$ is indeed not necessarily positive definite as already reported in [3, 20]. The values of these four invariants for 3 specific surface orientations $\{100\}$, $\{110\}$ and $\{111\}$ of all the 7 studied materials are presented in Table B.4-B.7 in Appendix B.

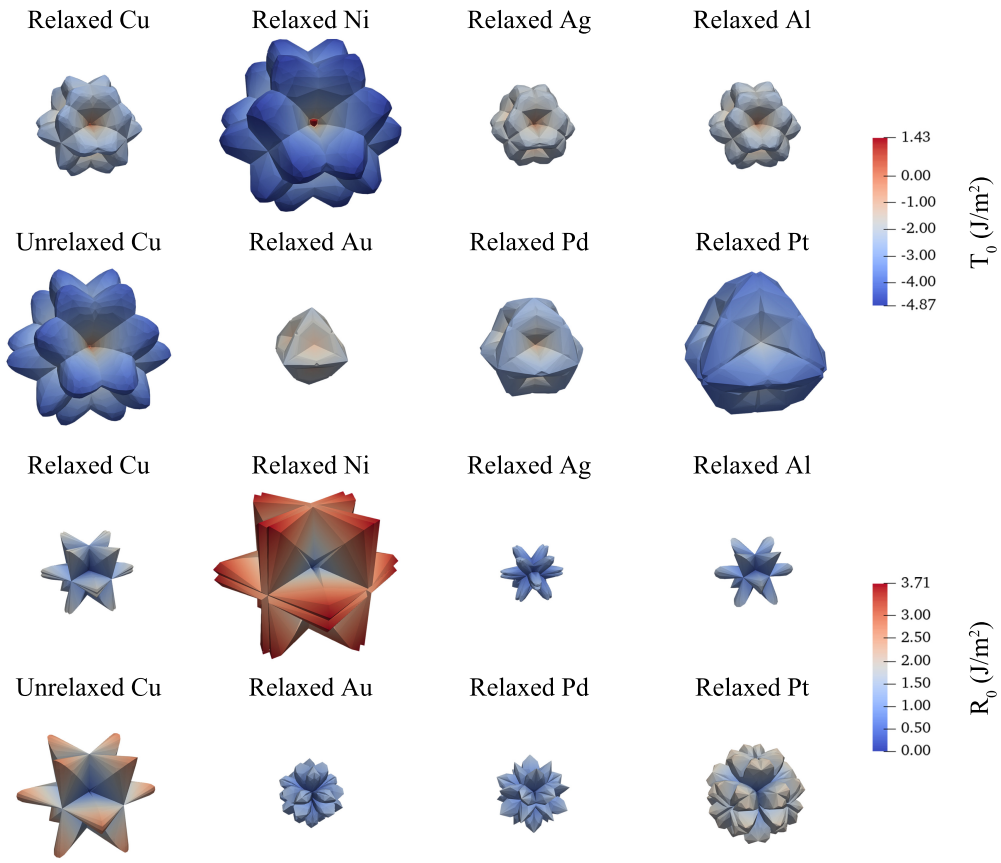

Figure 9: 3D surface plots of surface elastic stiffness non-angular invariants T_0 and R_0 for the 7 studied materials. For a sake of clarity, the coordinates axis are omitted but are at the same positions as shown in Figs. 6 (a-b). The size of these 3D plots is proportional to the corresponding amplitude of the stiffness invariants. Regarding the negative values for T_0, due to the center symmetry of FCC structure, the results are represented by their amplitude in the same crystallographic orientation and with the corresponding color defined in the colorbar.

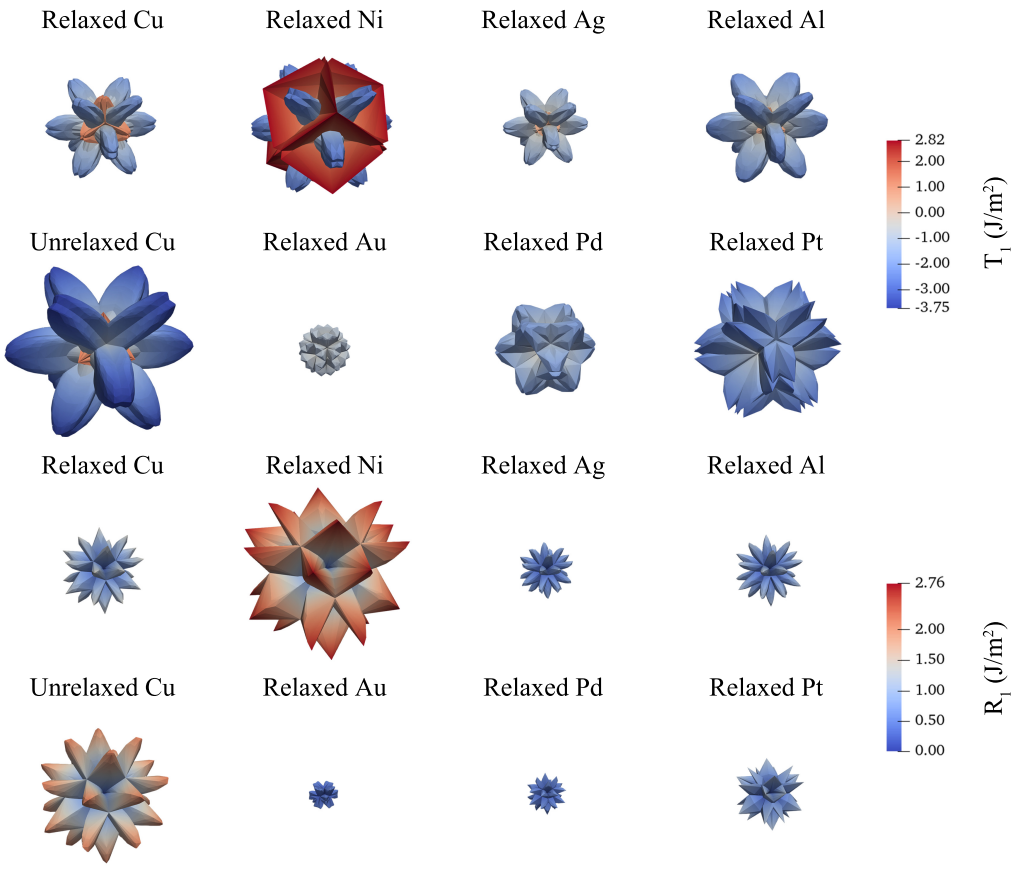

Figure 10: 3D surface plots of surface elastic stiffness non-angular invariants T_1 and R_1 for the 7 studied materials. For a sake of clarity, the coordinates axis are omitted but are at the same positions as shown in Figs. 6 (a-b). The size of these 3D plots is proportional to the corresponding amplitude of the stiffness invariants. Regarding the negative values for T_1, due to the center symmetry of FCC structure, the results are represented by their amplitude in the same crystallographic orientation and with the corresponding color defined in the colorbar.

5.1.4. Surface elastic angular invariants: $\Phi_1 - \Phi$ *and* $\Phi_0 - \Phi_1$

The distributions of surface elastic angular invariants $\Phi_1 - \Phi$ and $\Phi_0 - \Phi_1$ are presented in Fig. 11. The distribution of $\Phi_1 - \Phi$ has sharp variations between the values close to $-90°$ and the ones close to $90°$. However, based on previous analyses in Fig. 2, the case $\Phi_1 - \Phi$ close to $-90°$ should be similar as the case $\Phi_1 - \Phi$ close to $90°$. Similarly, $\Phi_0 - \Phi_1$ has sharp variations between the values close to $-45°$ and the ones close to $45°$ for the same reason.

Meanwhile, $\Phi_1 - \Phi$ displays similar forms between different materials except for Ag ($\Phi_1 - \Phi \approx 0°$ for most surface orientations), even considering surface relaxation effects. However, $\Phi_0 - \Phi_1$ shows stronger differences between different materials. Furthermore, both of these two angular invariants show clear anisotropic behaviors. The values of these two angular invariants for 3 specific surface orientations {100}, {110} and {111} of all the 7 studied materials are presented in Table B.8-B.9 in Appendix B.

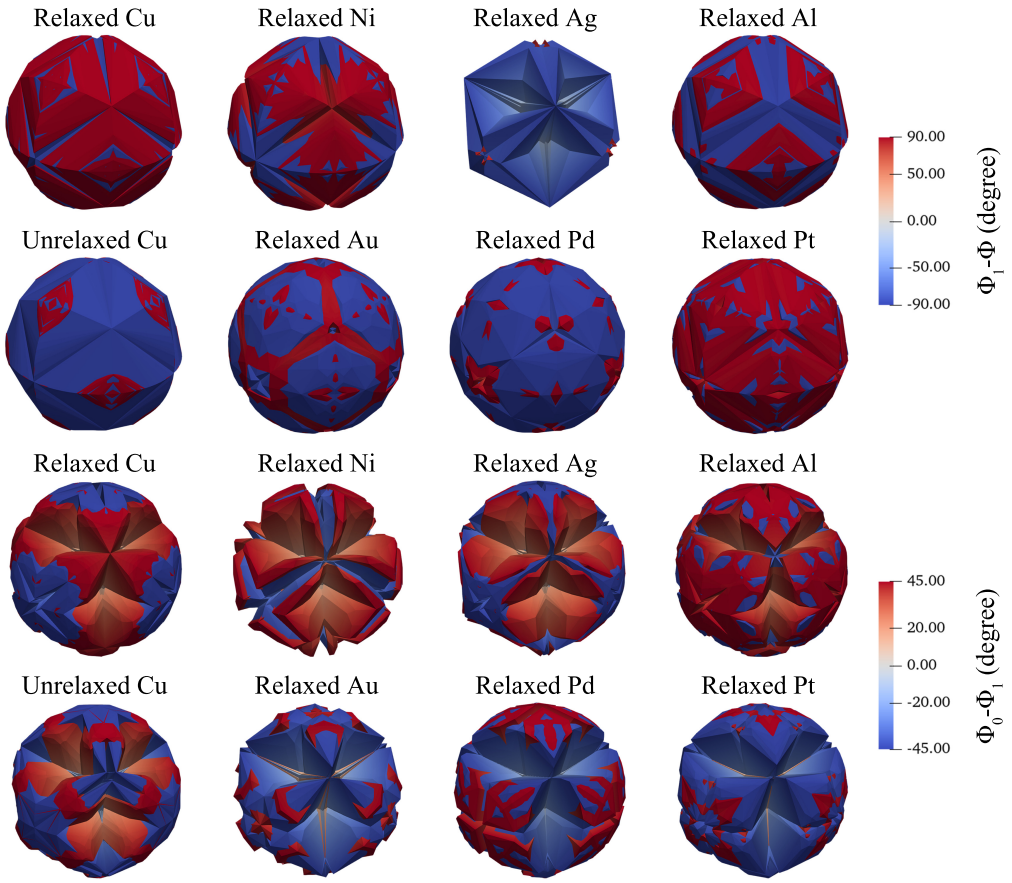

Figure 11: 3D surface plots of surface elastic angular invariants for the 7 studied materials. For a sake of clarity, the coordinates axis are omitted but are at the same positions as shown in Figs. 6 (a-b). The size of these 3D plots is proportional to the corresponding amplitude of the angular invariants. Regarding the negative values, due to the center symmetry of FCC structure, the results are represented by their amplitude in the same crystallographic orientation and with the corresponding color defined in the colorbar.

5.2. Predicting invariant surface elastic properties via machine learning methods

5.2.1. Predicting invariant surface elastic properties using the ANN method

The ANN method described in Sub-section 4.1 was used to construct a regression model which predicts the invariant surface elastic properties for each studied material with respect to crystallographic surface orientations without MS simulation. In order to evaluate the accuracy of these ANN models, the coefficient of determination (R2) was used as the error score. The predictions from ANN regression models for surface elastic non-angular parameters compared to the results obtained by the semi-analytical method on the testing set are presented in Fig. 12. It can be found that the developed ANN regression models well predict surface elastic non-angular parameters as the predictions have excellent error scores.

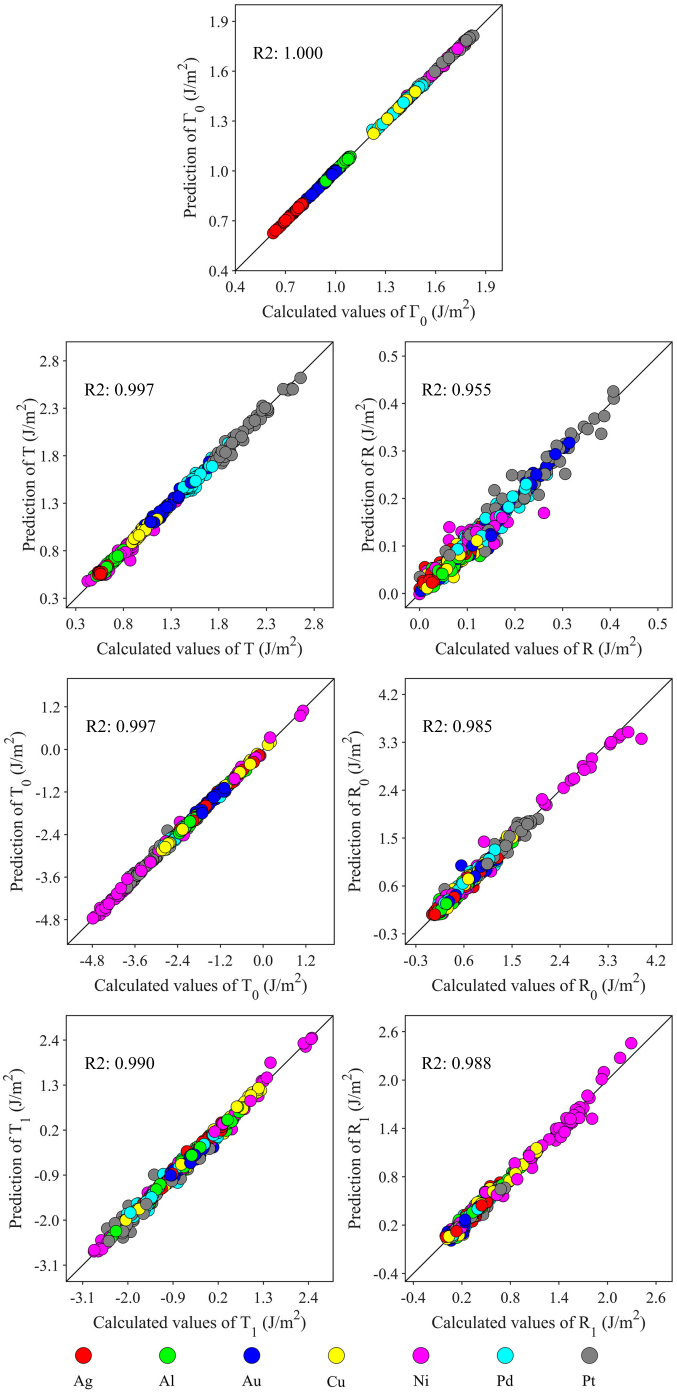

Figure 12: Predictions from 2 hidden layer × 5 neurons ANN regression models vs calculated results of surface elastic non-angular parameters and the corresponding error score.

Regarding the surface elastic angular parameters, in order to remove the influence of circular data on the schematic representation, the results are represented by the relative difference between the predictions and the calculated results as shown in Figs. 13 (a-b) with the corresponding error score. The relative difference of an angular data is defined as the angular difference between two angles in the polar coordinates as schematically shown in Figs. 13 (c-d). It can be found out that the predictions are better for $\Phi_1 - \Phi$ than for $\Phi_0 - \Phi_1$. From Fig. 11, it is observed that the apparently sharp variation of $\Phi_0 - \Phi_1$ is more complex to handle than for $\Phi_1 - \Phi$, which makes the predictions more difficult. Moreover, the discrete-classification conversion method used is known to exhibit a precision loss problem (see Sub-section 4.1) [47], which can reduce the accuracy of the predictions. After a systematic comparative study, we found that improving the classification precision (increasing the values of N and M) and extending the database can increase the predictive accuracy. Even if there are discretization and some accuracy problems, the predictions of the present models are still acceptable regarding the error scores.

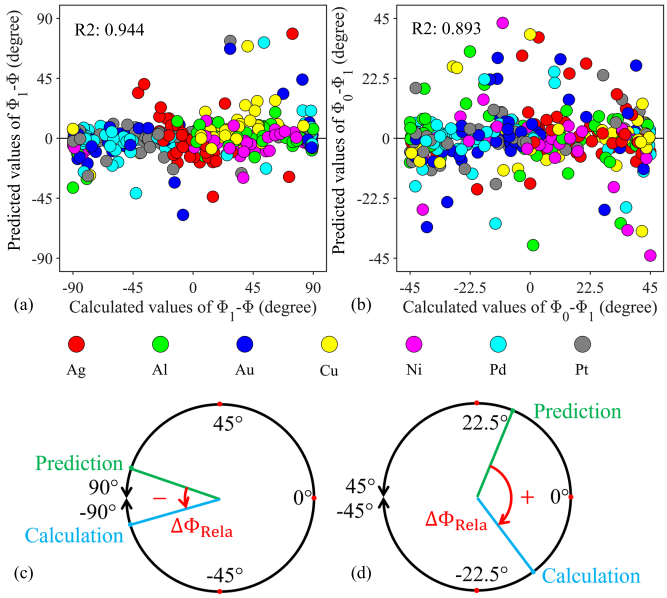

Figure 13: Relative difference between the predictions and the calculated results for the angular parameters: (a) $\Phi_1 - \Phi$ and (b) $\Phi_0 - \Phi_1$ with the corresponding error score. Schematic figures for the definition of the relative difference $\Delta\Phi_{\text{Rela}}$ for: (c) $\Phi_1 - \Phi$ and (d) $\Phi_0 - \Phi_1$.

5.2.2. Predictions and analyses of the importance of factors for surface elastic non-angular parameters using the BRT approach

For comparison, the BRT approach described in Sub-section 4.2 was also used to construct regression models for predicting each surface elastic non-angular parameter for the studied materials without MS simulation. Interestingly, Fig. 14 shows that the BRT regression models are as accurate as the developed ANN regression models for all the surface elastic non-angular parameters.

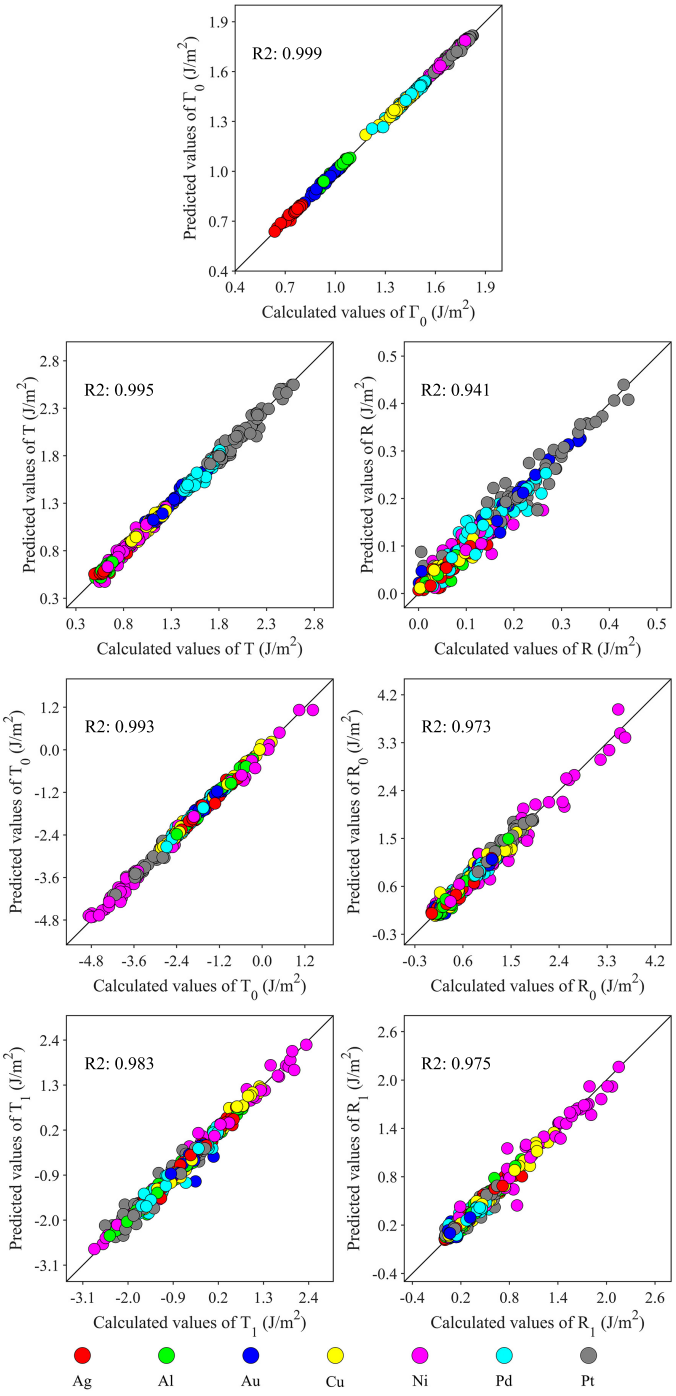

Figure 14: Cross-validated predictions vs calculated results of surface elastic non-angular parameters with the corresponding error score using the BRT models.

As discussed in Sub-section 4.2, the importance score of each input factor was also analyzed with the BRT models. The importance scores of all the 9 input factors for each surface elastic non-angular parameter are presented in Fig. 15. It can be found that the importance of each factor is not the same. For example, it is observed that Γ_0 is strongly influenced by G'', a and SFE. This observation means that Γ_0 will exhibit a clear difference between two materials if their G'' or/and a or/and SFE are different. Then, it is interesting to note that T is mainly influenced by K and A. Meanwhile, K and A also have influences on R, while the other surface elastic non-angular parameters are not significantly influenced by them. These results indicate that the bulk modulus and the elastic anisotropy of the material only have a significant influence on the residual surface stress tensor. Moreover, R is reasonably influenced by the surface orientation. Concerning $\mathbb{C}^{\mathrm{S}}_{\alpha\beta\kappa\lambda}$, both isotropic ($T_0$ and T_1) and anisotropic (R_0 and R_1) parts are significantly influenced by the surface orientation, which confirms that these surface elastic invariants are strongly anisotropic (cf. Fig. 9-10). It is also noteworthy that the cohesive energy seems to display a non-negligible influence on several parameters, in particular on T_0 and R_0. Finally, we point out that the developed BRT models only work well for the materials that are already in the training set due to the small quantity of considered materials (only 7 metals).

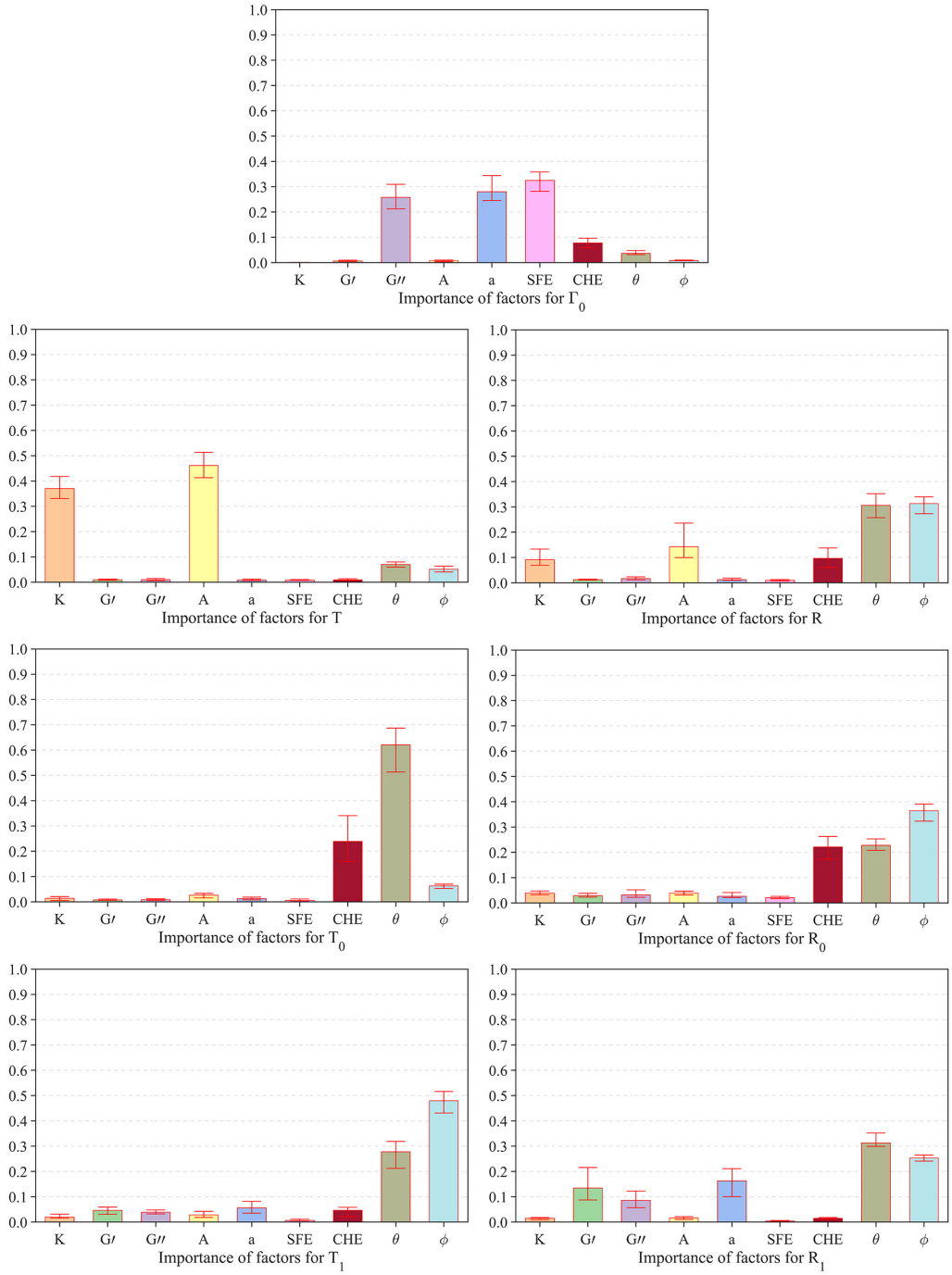

Figure 15: Importance analyses of the input factors used in the BRT models for predictions of surface elastic non-angular parameters.

5.3. Variation of the surface excess energy density Γ *for a given strain loading*

Based on Eq. (24), the surface excess energy density Γ for a given in-plane strain can be expressed only with respect to the invariant surface elastic properties. Then, combined with ANN machine-learned models for the predictions of these properties, Γ can be rapidly determined for a given in-plane strain loading and a given surface of any material in the database. In the present section, both surface elastic non-angular and angular parameters are predicted by the ANN models, which are individually trained for each material as described in Sub-section 4.1. In order to evaluate the accuracy of Γ prediction, the root mean squared error (RMSE) was used as the error score.

5.3.1. Verification of the predicted Γ *values from the ANN based models*

First of all, we evaluated the variation of the surface excess free energy density, Γ, for 6 different strain loading paths from the predicted parameters (cf. Eqs. (26)-(30)). These results were compared with those obtained from parameters directly calculated by the semi-analytical approach for 595 Cu surfaces (see Fig. 16 (d)) which are not in the database described in Fig. 3 (a). Among all of the considered configurations ($595 \times 6 = 3570$ configurations in total), Fig. 16 (a) shows the results with the best RMSE score, which is the shear deformation along the first principal direction of $\Sigma^0_{\alpha\beta}$ on the $[0.95, 0.29, 0.08]$-oriented surface (in this configuration, the positive shear and the negative shear give the same results, see more details in Subsection 5.3.2). The predicted values of Γ agree almost perfectly with the ones calculated by the semi-analytical method. Then, Fig. 16 (b) shows the result with the worst RMSE score, which is equibiaxial tensile strains along the two principal directions of $\Sigma^0_{\alpha\beta}$ on the $\{112\}$ surface. However, our predictions have the same trend compared to the calculated result, but with a small constant difference about 0.025 J/m^2 coming from the Γ_0 prediction. Furthermore, Fig. 16 (c) shows a case where the prediction has a different trend compared to the calculated result. This case corresponds to the shear deformation along the first principal direction of $\Sigma^0_{\alpha\beta}$ on the $[0.61, 0.61, 0.50]$-oriented surface (the positive shear and the negative shear give the same results). Even though the prediction displays a different trend, the difference remains very small, *i.e.* about 0.014% until a strain magnitude $\varepsilon = 0.01$. It should be pointed out that these positive/negative shear deformations are the only two cases with a different tendency among all the 3570 considered configurations. Figure 16 (e) presents the statistical distribution of RMSE

scores for all the considered configurations with $\varepsilon \in [0, 0.01]$. We observe that nearly all the configurations have a RMSE score smaller than 3×10^{-2} J/m^2, which is an acceptable error score compared to the general value of Γ (about 1 J/m^2). Based on the previous analyzes, these results indicate that the prediction of Γ by machine-learned models is acceptable.

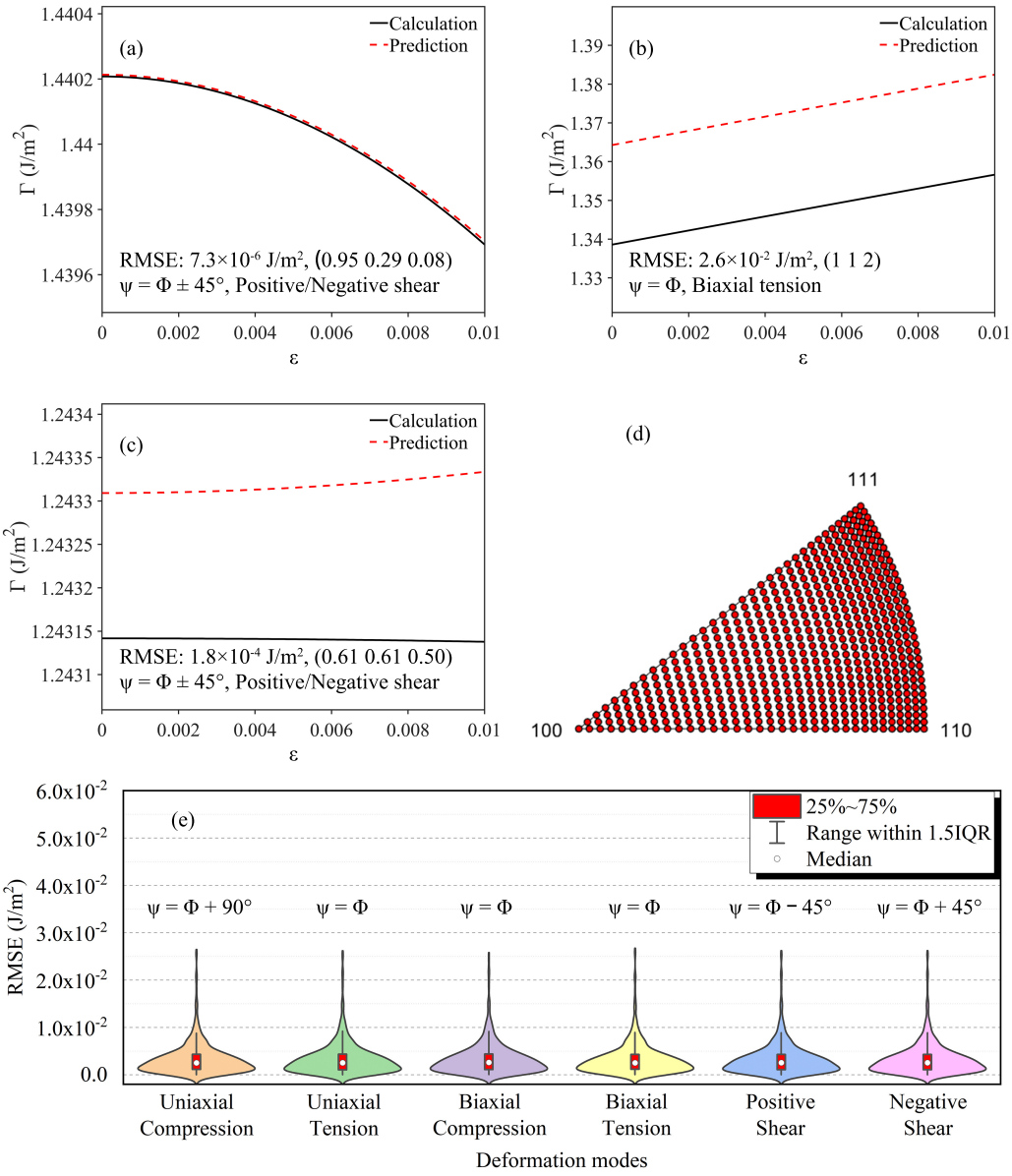

Figure 16: Comparison between the predicted evolution of Γ and the calculated one (see Eqs. (3) and (24)) with : (a) the best RMSE score, (b) the worst RMSE score and (c) the inverse tendency, among 595 verified Cu surfaces (see Fig. (d)) and 6 deformation modes. (d) 595 uniform surface orientations presented in the IPF. (e) The distribution of RMSE scores of 595 verified Cu surfaces (see Fig. (d)) and 6 deformation modes with $\varepsilon \in [0, 0.01]$.

5.3.2. Evaluation of Γ *with different deformation modes and discussion*

Based on Eq. (24) and ANN machine-learned models, the effects of different in-plane strain modes on Γ were analyzed. The strain magnitude ε was considered as a small value for only considering elasticity at small strains.

First, the case of uniaxial compressive and tensile strains along the first principal direction of $\Sigma^0_{\alpha\beta}$ was considered. For a low strain magnitude ε, Eq. (24) can be approximated as $\Gamma \approx \Gamma_0 - (T + R)\,\varepsilon$ for an uniaxial compressive strain with $\psi = \Phi + 90°$ and $\Gamma \approx \Gamma_0 + (T + R)\,\varepsilon$ for an uniaxial tensile strain with $\psi = \Phi$, as the second-order terms in ε can be neglected. Thus, Γ mainly depends on the contribution of $\Sigma^0_{\alpha\beta}$. Meanwhile, since T and R are always positive for all the surface orientations (see Fig. 8), Γ decreases for a compressive strain and increases for a tensile strain in an approximate linear relationship, which is consistent with the findings in Sub-section 5.1.2.

Then, with an equibiaxial strains mode (compressive or tensile), Eq. (24) is reduced to $\Gamma = \Gamma_0 - 2T\varepsilon + 4T_1\varepsilon^2$ for compressive strains and $\Gamma = \Gamma_0 + 2T\varepsilon + 4T_1\varepsilon^2$ for tensile strains, *i.e.* Γ is independent of ψ which is related to the principal directions of the applied strain loading. Moreover, for a low strain magnitude ε, Eq. (24) can be further approximated as $\Gamma \approx \Gamma_0 - 2T\varepsilon$ for compressive strains and $\Gamma \approx \Gamma_0 + 2T\varepsilon$ for tensile strains by neglecting the second-order terms in ε. Therefore, similar to the uniaxial strain modes, Γ mainly depends on the contribution of $\Sigma^0_{\alpha\beta}$. Hence, Γ decreases for equibiaxial compressive strains and increases for equibiaxial tensile strains in an approximate linear relationship. The independence of Γ with respect to the in-plane strain direction and its approximate linear variation with the applied strain magnitude ε were verified by molecular dynamics simulations for the equibiaxial compressive strains mode on $\{100\}$ Cu surface with $\varepsilon \in [0, 0.01]$.

Finally, considering a shear deformation along the first principal direction of $\Sigma^0_{\alpha\beta}$, Eq. (24) is reduced to $\Gamma = \Gamma_0 + 2\left[R_0 \cos 4\left(\Phi_0 - \psi\right) + T_0\right]\varepsilon^2$ (see Eq. (30)). Therefore, unlike the previous results with compressive or tensile strain modes, the residual surface stress tensor $\Sigma^0_{\alpha\beta}$ does not have any influence on Γ. However, in this case, the amplitude of the Γ variation remains very small (about 0.02% to 0.05% for ε within $[0, 0.01]$). Furthermore, the term $R_0 \cos 4\left(\Phi_0 - \psi\right)$ is the same for a positive shear or a negative shear, or by changing ψ by $\psi + 90°$. That means that Γ exhibits the same response for a positive or a negative shear. However, it should be pointed out that for a shear deformation along other directions, positive and negative shears will induce different evolution of Γ.

6. Conclusions and perspectives

In this contribution, the invariant surface elastic properties of 7 FCC metals (Ag, Al, Au, Cu, Ni, Pd and Pt) were studied by using a semi-analytical method based on Molecular Static (MS) simulations. A quite large database obtained from these numerical simulations and associated with machined-learning methods were used to develop surrogate models and investigate possible connections between surface and bulk elastic properties coming from the database. Specifically, the surface elastic behavior can be fully characterized by 9 properties which are invariant by rotation.

The distributions of these invariant properties were computed by the semi-analytical method and represented in 3D views showing clear anisotropic behaviors. The forms of the intrinsic surface excess energy density Γ_0 in 3D views are found to be similar but not homothetic. Considering the forms of the other surface elastic non-angular parameters (T, R, T_0, R_0, T_1 and R_1), the 7 studied materials can be roughly classified into two groups with a similar form for each invariant, whereas their forms always exhibit different magnitudes. In particular, it is observed that T, the spherical part of the residual surface stress tensor $\Sigma^0_{\alpha\beta}$, is positive for all the surface orientations among different materials, which means the free surface is always in a tensile state.

In addition, the ANN approach was used to predict the invariant surface elastic properties for both non-angular and angular parameters with respect to the surface orientation without the need of complex atomistic simulations. The results showed that the developed ANN models work well for the studied 7 FCC metals. Then, the BRT approach was also considered for analyzing the importance score of the material's bulk properties for surface elastic non-angular parameters. In particular, it was observed that T has clear correlations with the bulk modulus K and the elastic anisotropy ratio A of the material, while R, the anisotropic part of $\Sigma^0_{\alpha\beta}$, is reasonably influenced by the surface crystallographic orientation.

The surface excess energy density Γ was expressed by a simple formula only based on invariant surface elastic properties for a given in-plane strain. Therefore, combined with the developed ANN models, a fast evaluation of Γ can be performed for any in-plane deformation mode. The predicted evolutions of Γ from the developed ANN models were reasonable regarding the RMSE scores compared to the calculated evolutions using the semi-analytical method. Meanwhile, at small applied strains, the contribution of the surface

elastic stiffness tensor $\mathbb{C}^{\mathrm{S}}_{\alpha\beta\kappa\lambda}$ appears negligible for uniaxial/equibiaxial tensile/compressive strain modes compared to the one of the residual surface stress tensor $\Sigma^{0}_{\alpha\beta}$. In the case of an equibiaxial strain mode (compressive or tensile mode), the variation of Γ is independent of the in-plane deformation direction.

Further studies can investigate the case of surface properties of body-centered cubic (BCC) / hexagonal close packed (HCP) metals with the same methodology based on the determination of invariants by rotation and the use of machine learning methods (ANN and BRT). Besides, a much larger quantity of materials would have to be considered in the training set in order to possibly achieve the building of a universal predictive model of surface elastic properties working for any crystalline material.

Supplementary materials

The ANN based Matlab code used to determine the evaluation of the surface excess energy density Γ as a function of a given in-plane strain as described in Sub-section 3.1, as well as the used database described in Sub-section 4.1 are provided at `https://github.com/AniPlas/SurfElaInvML`. Then, the developed Python code for the BRT models is also provided, which is based on the boosting algorithm AdaBoost [53] in *Scikit-learn* [54] as described in Sub-section 4.2. Meanwhile, the final BRT models with the best five-fold cross-validated hyperparameters (listed in Table 1) are provided in the form of pkl.

CRediT authorship contribution statement

X. Chen: Conceptualization, Methodology, Software, Validation, Formal analysis, Investigation, Data Curation, Writing - Original Draft, Visualization, Writing - Review & Editing **R. Dingreville:** Conceptualization, Methodology, Software, Validation, Formal analysis, Data Curation, Writing - Original Draft, Writing - Review & Editing **T. Richeton:** Conceptualization, Methodology, Software, Validation, Formal analysis, Data Curation, Writing - Review & Editing **S. Berbenni:** Conceptualization, Methodology, Software, Validation, Formal analysis, Resources, Data Curation, Writing - Review & Editing

Acknowledgements

X.C., T.R., and S.B. are grateful to the French State (ANR) through the program "Investment in the future" (LabEx "DAMAS" referenced as ANR-11-LABX- 0008-01) for financial supports. R.D. is supported by the Center for Integrated Nanotechnologies, an Office of Science user facility operated for the U.S. Department of Energy. Sandia National Laboratories is a multi-mission laboratory managed and operated by National Technology and Engineering Solutions of Sandia, LLC., a wholly owned subsidiary of Honeywell International, Inc., for the U.S. Department of Energy National Nuclear Security Administration under contract DE-NA0003525. The views expressed in the article do not necessarily represent the views of the U.S. Department of Energy or the United States Government.

Appendix A. Polar components of surface elastic tensorial properties

Based on Eqs. (19)-(20), the explicit expressions of the polar components for $\Sigma^0_{\alpha\beta}$ and $\mathbb{C}^{\mathrm{S}}_{\alpha\beta\kappa\lambda}$ can be resolved based on their Cartesian components as follows: [37].

$$\begin{aligned} T &= \frac{\Sigma^0_{11}+\Sigma^0_{22}}{2} \\ R &= \sqrt{\left(\frac{\Sigma^0_{11}-\Sigma^0_{22}}{2}\right)^2+{\Sigma^0_{12}}^2} \end{aligned} \tag{A.1}$$

$$\Phi = \frac{1}{2}\mathrm{atan2}\left(2\Sigma^0_{12},\Sigma^0_{11}-\Sigma^0_{22}\right) \tag{A.2}$$

$$\begin{aligned} T_0 &= \frac{\mathbb{C}^{\mathrm{S}}_{1111}-2\mathbb{C}^{\mathrm{S}}_{1122}+4\mathbb{C}^{\mathrm{S}}_{1212}+\mathbb{C}^{\mathrm{S}}_{2222}}{8} \\ T_1 &= \frac{\mathbb{C}^{\mathrm{S}}_{1111}+2\mathbb{C}^{\mathrm{S}}_{1122}+\mathbb{C}^{\mathrm{S}}_{2222}}{8} \\ R_0 &= \sqrt{\left(\frac{\mathbb{C}^{\mathrm{S}}_{1112}-\mathbb{C}^{\mathrm{S}}_{2212}}{2}\right)^2+\left(\frac{\mathbb{C}^{\mathrm{S}}_{1111}-2\mathbb{C}^{\mathrm{S}}_{1122}-4\mathbb{C}^{\mathrm{S}}_{1212}+\mathbb{C}^{\mathrm{S}}_{2222}}{8}\right)^2} \\ R_1 &= \sqrt{\left(\frac{\mathbb{C}^{\mathrm{S}}_{1112}+\mathbb{C}^{\mathrm{S}}_{2212}}{4}\right)^2+\left(\frac{\mathbb{C}^{\mathrm{S}}_{1111}-\mathbb{C}^{\mathrm{S}}_{2222}}{8}\right)^2} \end{aligned} \tag{A.3}$$

$$\begin{aligned} \Phi_1 &= \frac{1}{2}\mathrm{atan2}\left(2\left(\mathbb{C}^{\mathrm{S}}_{1112}+\mathbb{C}^{\mathrm{S}}_{2212}\right),\mathbb{C}^{\mathrm{S}}_{1111}-\mathbb{C}^{\mathrm{S}}_{2222}\right) \\ \Phi_0 &= \frac{1}{4}\mathrm{atan2}\left(4\left(\mathbb{C}^{\mathrm{S}}_{1112}-\mathbb{C}^{\mathrm{S}}_{2212}\right),\mathbb{C}^{\mathrm{S}}_{1111}+\mathbb{C}^{\mathrm{S}}_{2222}-2\mathbb{C}^{\mathrm{S}}_{1122}-4\mathbb{C}^{\mathrm{S}}_{1212}\right) \end{aligned} \tag{A.4}$$

where $\mathrm{atan2}\,(y,x)$ is the 2-argument arctangent function, which gives an unique solution for the arc-tangent function in the range $]-180°, 180°]$.

Appendix B. Invariant surface elastic properties of low-index surfaces

		Ag	Al	Au	Cu	Ni	Pd	Pt
Γ_0	{111}	0.62	0.91	0.79	1.18	1.45	1.22	1.43
		$0.62^{(a)}$			$1.18^{(a)}$	$1.44^{(a)}$	$1.22^{(a)}$	
	{100}	0.70	0.97	0.92	1.31	1.57	1.36	1.62
		$0.70^{(a)}$			$1.29^{(a)}$	$1.57^{(a)}$	$1.38^{(a)}$	
	{110}	0.76	1.05	0.98	1.41	1.70	1.48	1.74
		$0.77^{(a)}$			$1.41^{(a)}$	$1.72^{(a)}$	$1.48^{(a)}$	
	$\frac{\{110\}}{\{111\}}$	1.24	1.16	1.24	1.19	1.18	1.21	1.22
		$1.24^{(a)}$			$1.20^{(a)}$	$1.20^{(a)}$	$1.21^{(a)}$	

Table B.1: Values of Γ_0 in J/m^2 for {111}, {100} and {110} surfaces computed with the semi-analytical method. Comparisons with values (a) obtained in [20].

		Ag	Al	Au	Cu	Ni	Pd	Pt
T	{111}	0.62	0.41	1.69	0.86	0.39	1.95	2.77
	{100}	0.84	0.92	1.57	1.49	1.35	2.00	2.59
	{110}	0.57	0.61	1.25	1.04	0.83	1.51	1.83

Table B.2: Values of T in J/m^2 for {111}, {100} and {110} surfaces computed with the semi-analytical method.

		Ag	Al	Au	Cu	Ni	Pd	Pt
R	{111}	0.00	0.04	0.00	0.02	0.01	0.02	0.03
	{100}	0.00	0.00	0.01	0.04	0.00	0.00	0.04
	{110}	0.10	0.10	0.31	0.06	0.16	0.19	0.41

Table B.3: Values of R in J/m^2 for {111}, {100} and {110} surfaces computed with the semi-analytical method.

		Ag	Al	Au	Cu	Ni	Pd	Pt
T_0	{111}	-0.12	0.18	-0.94	0.50	1.43	-1.07	-1.91
	{100}	-2.02	-1.91	-2.30	-2.37	-3.43	-2.85	-4.06
	{110}	-2.03	-2.26	-1.80	-2.53	-4.04	-2.67	-3.58

Table B.4: Values of T_0 in J/m^2 for {111}, {100} and {110} surfaces computed with the semi-analytical method.

		Ag	Al	Au	Cu	Ni	Pd	Pt
R_0	{111}	0.01	0.25	0.15	0.13	0.09	0.14	0.21
	{100}	0.34	0.72	0.88	1.01	2.50	0.54	1.29
	{110}	1.17	1.58	0.22	1.82	3.49	0.75	0.95

Table B.5: Values of R_0 in J/m^2 for {111}, {100} and {110} surfaces computed with the semi-analytical method.

		Ag	Al	Au	Cu	Ni	Pd	Pt
T_1	{111}	0.57	0.35	-0.36	0.80	2.82	-1.02	-1.45
	{100}	0.56	0.75	-0.34	1.13	2.49	-0.05	-0.62
	{110}	-1.55	-2.44	-0.38	-2.12	-2.68	-1.87	-2.17

Table B.6: Values of T_1 in J/m^2 for {111}, {100} and {110} surfaces computed with the semi-analytical method.

		Ag	Al	Au	Cu	Ni	Pd	Pt
R_1	{111}	0.01	0.11	0.08	0.04	0.03	0.06	0.07
	{100}	0.00	0.00	0.05	0.14	0.00	0.00	0.10
	{110}	0.35	0.40	0.43	0.68	1.71	0.32	0.59

Table B.7: Values of R_1 in J/m^2 for {111}, {100} and {110} surfaces computed with the semi-analytical method.

		Ag	Al	Au	Cu	Ni	Pd	Pt
$\Phi_1 - \Phi$	{111}	-88.1	-89.6	-84.2	89.4	83.6	-84.8	81.0
	{100}	-82.0	-90.0	-46.5	-87.7	-90.0	-68.4	83.5
	{110}	-3.0	90.0	87.6	90.0	-89.8	90.0	85.4

Table B.8: Values of $\Phi_1 - \Phi$ in degree for {111}, {100} and {110} surfaces computed with the semi-analytical method.

		Ag	Al	Au	Cu	Ni	Pd	Pt
$\Phi_0 - \Phi_1$	{111}	15.6	-18.4	39.2	42.4	10.7	6.5	9.2
	{100}	-20.8	-0.0	19.1	-2.0	-0.0	32.9	-40.0
	{110}	1.0	-0.0	3.4	-0.0	-0.0	-0.0	1.4

Table B.9: Values of $\Phi_0 - \Phi_1$ in degree for {111}, {100} and {110} surfaces computed with the semi-analytical method.

References

[1] J.W. Gibbs. *The Collected Works of J. Willard Gibbs, Volume I: Thermodynamics*. Yale University Press, 1928.

[2] R.E. Miller and V.B. Shenoy. Size-dependent elastic properties of nanosized structural elements. *Nanotechnology*, 11(3):139, 2000. doi: 10.1088/0957-4484/11/3/301.

[3] R. Dingreville, J. Qu, and M. Cherkaoui. Surface free energy and its effect on the elastic behavior of nano-sized particles, wires and films. *J. Mech. Phys. Solids*, 53(8):1827–1854, 2005. doi: 10.1016/j.jmps.2005.02.012.

[4] P.R. Couchman and W.A. Jesser. Thermodynamic theory of size dependence of melting temperature in metals. *Nature*, 269(5628):481–483, 1977. doi: 10.1038/269481a0.

[5] G. Guisbiers, M. Kazan, O. Van Overschelde, M. Wautelet, and S. Pereira. Mechanical and thermal properties of metallic and semiconductive nanostructures. *J. Phys. Chem. C*, 112(11):4097–4103, 2008. doi: 10.1021/jp077371n.

[6] R.J. Needs, M.J. Godfrey, and M. Mansfield. Theory of surface stress and surface reconstruction. *Surf. Sci.*, 242(1-3):215–221, 1991. doi: 10.1016/0039-6028(91)90269-X.

[7] H. Ibach. The role of surface stress in reconstruction, epitaxial growth and stabilization of mesoscopic structures. *Surf. Sci. Rep.*, 29(5-6):195–263, 1997. doi: 10.1016/S0167-5729(97)00010-1.

[8] G.Y. Chen, T. Thundat, E.A. Wachter, and R.J. Warmack. Adsorption-induced surface stress and its effects on resonance frequency of microcantilevers. *J. Appl. Phys.*, 77(8):3618–3622, 1995. doi: 10.1063/1.359562.

[9] W. Haiss. Surface stress of clean and adsorbate-covered solids. *Rep. Prog. Phys.*, 64(5):591, 2001. doi: 10.1088/0034-4885/64/5/201.

[10] J. Biener, A. Wittstock, L.A. Zepeda-Ruiz, M.M. Biener, V. Zielasek, D. Kramer, R.N. Viswanath, J. Weissmüller, M. Bäumer, and A.V. Hamza. Surface-chemistry-driven actuation in nanoporous gold. *Nat. Mater.*, 8(1):47–51, 2009. doi: 10.1038/nmat2335.

[11] J. Diao, K. Gall, and M.L. Dunn. Surface-stress-induced phase transformation in metal nanowires. *Nat. Mater.*, 2(10):656–660, 2003. doi: 10.1038/nmat977.

[12] F.D. Fischer, T. Waitz, D. Vollath, and N.K. Simha. On the role of surface energy and surface stress in phase-transforming nanoparticles. *Prog. Mater. Sci.*, 53(3):481–527, 2008. doi: 10.1016/j.pmatsci.2007.09.001.

[13] B. Croset and C. de Beauvais. Self-organization of stressed surfaces: The role of local relaxations. *Phys. Rev. B*, 61(4):3039, 2000. doi: 10.1103/PhysRevB.61.3039.

[14] S. Rousset, V. Repain, G. Baudot, Y. Garreau, and J. Lecoeur. Self-ordering of au (111) vicinal surfaces and application to nanostructure organized growth. *J. Phys. Condens. Matter*, 15(47):S3363, 2003. doi: 10.1088/0953-8984/15/47/009.

[15] W.R. Tyson and W.A. Miller. Surface free energies of solid metals: Estimation from liquid surface tension measurements. *Surf. Sci.*, 62(1):267–276, 1977. doi: 10.1016/0039-6028(77)90442-3.

[16] G.Y. Jing, H.L. Duan, X.M. Sun, Z.S. Zhang, J. Xu, Y.D. Li, J.X. Wang, and D.P. Yu. Surface effects on elastic properties of silver nanowires: contact atomic-force microscopy. *Phys. Rev. B*, 73(23):235409, 2006. doi: 10.1103/PhysRevB.73.235409.

[17] J.E. Sader. Surface stress induced deflections of cantilever plates with applications to the atomic force microscope: Rectangular plates. *J. Appl. Phys.*, 89(5):2911–2921, 2001. doi: 10.1063/1.1342018.

[18] G.J. Ackland and M.W. Finnis. Semi-empirical calculation of solid surface tensions in body-centred cubic transition metals. *Philos. Mag. A*, 54(2):301–315, 1986. doi: 10.1080/01418618608242900.

[19] V.B. Shenoy. Atomistic calculations of elastic properties of metallic FCC crystal surfaces. *Phys. Rev. B*, 71(9):094104, 2005. doi: 10.1103/PhysRevB.71.094104.

[20] R. Dingreville and J. Qu. A semi-analytical method to compute surface elastic properties. *Acta Mater.*, 55(1):141–147, 2007. doi: 10.1016/j.actamat.2006.08.007.

[21] P. Vannucci. *Anisotropic Elasticity, Lecture Notes in Applied and Computational Mechanics 85*. Springer Nature Singapore Pte Ltd, 2018. doi: 10.1007/978-981-10-5439-6_1.

[22] G. Verchery. Les invariants des tenseurs d'ordre quatre du type de l'élasticité. In CNRS, editor, *Proceedings of the Euromech Colloquium 115*, 1982.

[23] R. Shuttleworth. The surface tension of solids. *Proc. Phys. Soc. Sect. A: Math. Phys. Eng. Sci.*, 63(5):444, 1950. doi: 10.1088/0370-1298/63/5/302.

[24] C. Herring. Surface tension as a motivation for sintering. In W. E. Kingston, editor, *The Physics of Powder Metallurgy*. McGraw-Hill, New York, 1951.

[25] M.E. Gurtin and A.I. Murdoch. A continuum theory of elastic material surfaces. *Arch. Ration. Mech. Anal.*, 57(4):291–323, 1975. doi: 10.1007/BF00261375.

[26] Murray S. Daw and M. I. Baskes. Semiempirical, quantum mechanical calculation of hydrogen embrittlement in metals. *Phys. Rev. Lett.*, 50:1285–1288, 1983. doi: 10.1103/PhysRevLett.50.1285.

[27] Murray S. Daw and M. I. Baskes. Embedded-atom method: Derivation and application to impurities, surfaces, and other defects in metals. *Phys. Rev. B*, 29:6443–6453, 1984. doi: 10.1103/PhysRevB.29.6443.

[28] S. Plimpton. Fast parallel algorithms for short-range molecular dynamics. *J. Comput. Phys.*, 117(1):1–19, 1995. doi: 10.1006/jcph.1995.1039.

[29] S. M. Foiles, M. I. Baskes, and M. S. Daw. Embedded-atom-method functions for the fcc metals Cu, Ag, Au, Ni, Pd, Pt, and their alloys. *Phys. Rev. B*, 33:7983–7991, 1986. doi: 10.1103/PhysRevB.33.7983.

[30] K.W. Jacobsen, J.K. Norskov, and M.J. Puska. Interatomic interactions in the effective-medium theory. *Phys. Rev. B*, 35(14):7423–7442, 1987. doi: 10.1103/physrevb.35.7423.

[31] Z. Wei, W. Ju, K. Bi, J. Yang, and Y. Chen. Significant enhancement of thermal boundary conductance in graphite/Al interface by ion intercalation. *Int. J. Heat Mass Transf.*, 157:119946, 2020. doi: 10.1016/j.ijheatmasstransfer.2020.119946.

[32] J. Wu, Z. Xu, L. Liu, A. Hartmaier, M. Rommel, K. Nordlund, T. Wang, R. Janisch, and J. Zhao. MD simulation study on defect evolution and doping efficiency of p-type doping of 3C-SiC by Al ion implantation with subsequent annealing. *J. Mater. Chem. C*, 9(7):2258–2275, 2021. doi: 10.1039/D0TC05374K.

[33] C. Balbuena, M.M. Gianetti, and E.R. Soulé. Molecular dynamics simulations of the formation of Ag nanoparticles assisted by PVP. *Phys. Chem. Chem. Phys.*, 23(11):6677–6684, 2021. doi: 10.1039/D1CP00211B.

[34] D.S. Bertoldi, E.N. Millán, and G.A. Fernández. Phenomenology of the heating, melting and diffusion processes in Au nanoparticles. *Phys. Chem. Chem. Phys.*, 23(2):1298–1307, 2021. doi: 10.1039/D0CP04442C.

[35] H. Mes-adi, K. Saadouni, and M. Mazroui. Effect of incident angle on the microstructure proprieties of Cu thin film deposited on Si (001) substrate. *Thin Solid Films*, 721:138553, 2021. doi: 10.1016/j.tsf.2021.138553.

[36] P. Vannucci. A special planar orthotropic material. *Journal of Elasticity*, 67:81–96, 2002. doi: 10.1023/A:1023949729395.

[37] P. Vannucci. Plane anisotropy by the polar method*. *Meccanica*, 40:437–454, 2005. doi: 10.1007/s11012-005-2132-z.

[38] P. Vannucci. A new general approach for optimizing the performances of smart laminates. *Mech. Adv. Mater. Struct.*, 18(7):548–558, 2011. doi: 10.1080/15376494.2011.605015.

[39] A. Catapano and M. Montemurro. A multi-scale approach for the optimum design of sandwich plates with honeycomb core. Part II: the optimisation strategy. *Compos. Struct.*, 118:677–690, 2014. doi: 10.1016/j.compstruct.2014.07.058.

[40] Md. Iqbal Quraishi, J Pal Choudhury, and Mallika De. Image recognition and processing using artificial neural network. In *2012 1st International Conference on Recent Advances in Information Technology (RAIT)*, pages 95–100, 2012. doi: 10.1109/RAIT.2012.6194487.

[41] Muhammad A. Panhwar, Kamran A. Memon, Adeel Abro, Deng Zhongliang, Sijjad A. Khuhro, and Saleemullah Memon. Signboard detection and text recognition using artificial neural networks. In *2019 IEEE 9th International Conference on Electronics Information and Emergency Communication (ICEIEC)*, pages 16–19, 2019. doi: 10.1109/ICEIEC.2019.8784625.

[42] K. Guo, Z. Yang, Chi-Hua Yu, and Markus J. Buehler. Artificial intelligence and machine learning in design of mechanical materials. *Mater. Horiz.*, 8:1153–1172, 2021. doi: 10.1039/D0MH01451F.

[43] L. Breiman, J. Friedman, C.J. Stone, and R.A. Olshen. *Classification and Regression Trees*. CRC press, 1984.

[44] R.E Schapire. The boosting approach to machine learning: An overview. In *Nonlinear Estimation and Classification*, pages 149–171. Springer, 2003.

[45] F. Rosenblatt. The perceptron: A probabilistic model for information storage and organization in the brain. *Psychol. Rev.*, 65(6):386–408, 1958. doi: 10.1037/h0042519.

[46] K. Hara and R. Chellappa. Growing regression tree forests by classification for continuous object pose estimation. *IJCV*, 2016. doi: arxiv.org/abs/1312.6430.

[47] K. Hara, R. Vemulapalli, and R. Chellappa. Designing deep convolutional neural networks for continuous object orientation estimation. *ArXiv e-prints*, 2017. doi: https://arxiv.org/abs/1702.01499.

[48] C. Bishop. *Pattern Recognition and Machine Learning*. Springer-Verlag New York, 2006.

[49] Matlab: Fit Data with a Shallow Neural Network. URL `https://ww2.mathworks.cn/help/deeplearning/gs/fit-data-with-a-neural-network.html?lang=en`.

[50] J. Elith, J.R Leathwick, and T. Hastie. A working guide to boosted regression trees. *J. Anim. Ecol.*, 77(4):802–813, 2008. doi: 10.1111/j.1365-2656.2008.01390.x.

[51] D. Montes de Oca Zapiain, M. Guziewski, S.P. Coleman, and R. Dingreville. Characterizing the tensile strength of metastable grain boundaries in silicon carbide using machine learning. *J. Phys. Chem. C*, 124(45):24809–24821, 2020. doi: 10.1021/acs.jpcc.0c07590.

[52] R. Dewit. Elastic constants and thermal expansion averages of a non textured polycrystal. *J. Mech. Mater. Struct*, 3(2):195–212, 2008. doi: 10.2140/jomms.2008.3.195.

[53] Y. Freund and R.E. Schapire. A decision-theoretic generalization of online learning and an application to boosting. *J. Comput. Syst. Sci*, 55 (1):119–139, 1997. doi: 10.1006/jcss.1997.1504.

[54] F. Pedregosa, G. Varoquaux, A. Gramfort, V. Michel, B. Thirion, O. Grisel, M. Blondel, P. Prettenhofer, R. Weiss, V. Dubourg, J. Vanderplas, A. Passos, D. Cournapeau, M. Brucher, M. Perrot, and E. Duchesnay. Scikit-learn: Machine learning in Python. *J. Mach. Learn. Res.*, 12:2825–2830, 2011. URL `http://jmlr.org/papers/v12/pedregosa11a.html`.

[55] C. Herring. Some theorems on the free energies of crystal surfaces. *Phys. Rev.*, 82(1):87, 1951. doi: 10.1103/PhysRev.82.87.

[56] R. Tran, Z. Xu, B. Radhakrishnan, D. Winston, W. Sun, K.A. Presson, and S.P. Ong. Surface energies of elemental crystals. *Scientific Data*, 3:160080, 2016. doi: 10.1038/sdata.2016.80.